

Article

Mineralogical and Geochemical Characteristics of the Deeply Buried Wufeng–Longmaxi Shale in the Southern Sichuan Basin, China: Implications for Provenance and Tectonic Setting

Ling Qi , Hongyan Wang, Zhensheng Shi * , Tianqi Zhou, Guizhong Li, Shasha Sun and Feng Cheng

Petrochina Research Institute of Petroleum Exploration and Development, Beijing 100083, China

* Correspondence: shizs69@petrochina.com.cn

Abstract: Uncertain provenance and tectonic setting of shale has constrained the exploration and exploitation of natural gas in the Wufeng–Longmaxi Formation in the southern Sichuan Basin, China. Therefore, this study analyzed the mineral petrology and geochemistry to assess the effects of sorting, recycling, weathering, and paleoclimate on the deeply buried shale. The findings revealed that the mineral composition is dominated by biogenic quartz, terrigenous clay minerals, and carbonate minerals. Combinations of clay lamina and silty lamina occur in black shale. The geochemical characteristics of these sedimentary rocks remain unaffected by sedimentary sorting and recycling processes. The clastic sediments primarily originate from the felsic igneous rock source that underwent moderate weathering during its initial deposition in the collision environment. Based on the comprehensive analysis of the paleoclimate and paleoprovenance characteristics, Wufeng–Longmaxi Formation characteristics are considered to have undergone six stages, among which the stage of relative enrichment of organic matter corresponds to LM1, LM2–3, and LM4. Following the Hirnantian glacial period, the era has witnessed global warming, marked by glacier melting, a rise in global sea level, and a decrease in terrestrial debris supply, collectively facilitating organic matter enrichment. During the LM5 and LM6–8 periods, the increase in source supply caused by the Leshan–Longnsvi and Qianzhong–Xuefeng uplift inhibited organic matter enrichment.

Keywords: provenance analysis; inorganic geochemistry; active tectonic settings; Wufeng Formation; Longmaxi Formation; southern Sichuan Basin



Citation: Qi, L.; Wang, H.; Shi, Z.; Zhou, T.; Li, G.; Sun, S.; Cheng, F. Mineralogical and Geochemical Characteristics of the Deeply Buried Wufeng–Longmaxi Shale in the Southern Sichuan Basin, China: Implications for Provenance and Tectonic Setting. *Minerals* **2023**, *13*, 1502. <https://doi.org/10.3390/min13121502>

Academic Editor: Luca Aldega

Received: 5 September 2023

Revised: 27 November 2023

Accepted: 28 November 2023

Published: 29 November 2023



Copyright: © 2023 by the authors. Licensee MDPI, Basel, Switzerland. This article is an open access article distributed under the terms and conditions of the Creative Commons Attribution (CC BY) license (<https://creativecommons.org/licenses/by/4.0/>).

1. Introduction

Global energy is shifting from fossil fuels to new energy sources, and natural gas, as the cleanest fossil fuel, can represent a bridge or an optimal partner for renewables [1]. Global shale gas reserves are abundant, with estimated geological resources of 1014 trillion m³ and extractable resources of 243 trillion m³ [2]. By 2022, the world will be producing 854.7 billion m³ of shale gas, which represents 21.2% of total global natural gas production [2]. China's shale gas production has had a remarkable growth trajectory over the past 8 years and reached an annual production value of 20 billion m³ [1]. The Wufeng–Longmaxi shale in southern Sichuan is a major stratum for shale gas exploration and exploitation. The geological reserve is estimated to be 6.6 trillion m³ [3]. The total organic carbon (TOC) content of the sediment can reach 10%, indicating good hydrocarbon generation potential [4,5]. Many factors control the variable TOC content in the depth interval. Previous research has shown that there was a transition in temperature from a cold state to a warm one throughout the Late Ordovician–Early Silurian period. This transition aligns with the presence of the Hirnantian Gondwana glacier [6,7].

The convergence of the Yangtze block and the Cathaysian block occurred as a result of the Guangxi movement, which transformed the Yangtze area from a passive continental margin basin to a foreland basin [8]. During the period from the Early Ordovician to the Middle Ordovician, the Yangtze area mainly experienced the formation and deposition

of carbonate platform sediments. Subsequently, since the Late Ordovician, extensive development of carbonate-clastic mixed deposits has occurred in the Yangtze region [9]. During the transition period from the Ordovician to the Silurian, the global sea level experienced considerable fluctuations. Consequently, a plethora of organisms such as radiolarians and siliceous sponges thrived, leading to a substantial increase in siliceous enrichment. The siliceous content of the Wufeng–Longmaxi Formation shale primarily has a biogenic origin, whereas carbonate minerals have predominantly biochemical or chemical origins. Previous research indicates that calcite formation occurs during the syngenetic rock stage or at the water sediment interface and during the early stages of diagenesis [10,11]. In contrast, Ferrodolomite is only formed during the later stages of diagenesis, whereas clay minerals mainly originate from terrigenous clastic sources [12].

The mineralogical, petrologic, and geochemical characteristics of black shales are diverse [13,14] and are significantly affected by their provenance, thereby effectively indicating the sorting, recycling, weathering, and depositional structure of the sediment source area [15–18]. The change in the chemical composition reflects the diagenetic transformation between different layers. The ratios of major elements and their oxides are typically used as the indicators of source rock mineralogy. Most of these rocks are derived from granite and sedimentary rocks [19]. The detrital sediments of the Wufeng–Longmaxi Formation possibly originated from the active continental margin [20,21].

In addition, the assessment of the proportion between stable and poor solubility elements is commonly determined by the source rock composition [22–24]. As the concentrations of elements such as Th, Sc, Zr, Hf, La, and Yb are relatively stable during sediment migration, they can be used to assess the provenance and tectonic setting of sediments [24–26].

Previous studies have extensively examined the climatic oscillations that occurred during the transition from the Ordovician to Silurian and the shift between anoxic and oxygenated conditions in marine waters [6,27,28]. It has been suggested that the sedimentary accumulation of the Wufeng–Longmaxi Formation was predominantly driven by tectonic processes and the conclusion of the Ordovician glaciation [6,20,26]. The rise in TOC levels was likely associated with the synergistic impacts of increased primary productivity and oxygen-depleted environments [29,30]. The provenance of the Wufeng–Longmaxi Formation mainly includes granite and sedimentary rocks [19]. The tectonic setting of the Upper Yangzi Plateau may have included both active and passive continental margins [25].

The research mentioned above relied on few shallow drilling wells and limited outcrop rock data. In this study, recent deep-drilling core samples were acquired, and they yielded a substantial quantity of precise geochemical data. Nonetheless, the transformation of organic matter and its influencing factors during sediment deposition in this region have not been explained comprehensively. Specifically, the sudden transition interface of the change process is not well defined. This manuscript extensively examines this issue. The specific objectives of this work include: (1) analyzing the lithology, laminae, organic matter distribution, and mineral compositional characteristics of shale; (2) evaluating the weathering and paleoclimate conditions prevalent in the shale source area of the Wufeng–Longmaxi Formation; (3) elucidating the source rock composition and diagenetic alteration; (4) determining the tectonic setting of the source area; and (5) providing evidence of the impact of terrestrial input on organic shale enrichment. Furthermore, the present study establishes a substantial basis for researching and implementing shale gas resources in the southern Sichuan Basin.

2. Geological Setting

Organic-rich shales were widely deposited in the southern Sichuan Basin during the Late Ordovician to Early Silurian (Katian–Rhuddanian) [17,18]. The shift from extension to extrusion conditions of the Yangtze and Cathaysia plates occurred in the beginning of the Late Ordovician period, mostly as a result of the Caledonian tectonic activity [8,31,32]. With the strengthening of the compressional collision, the marginal uplift zones of Leshan–

Longnsvi and Qianzhong–Xuefeng have continually expanded, and the relative sea level increased (Figure 1). The Yangtze region has transitioned from a passive continental margin carbonate platform sedimentary model to a foreland basin tectonic development stage. The entire Yangtze region forms a semi-closed, stagnant basin bounded by marginal uplift. The carbonate rock was replaced by black shale as the sedimentary strata evolved. The Yangtze Sea region has a steady increase in depth from the southeast to the north, characterized by a basin basement that is comparatively elevated in the southeastern portion and relatively lower in the northern area [33].

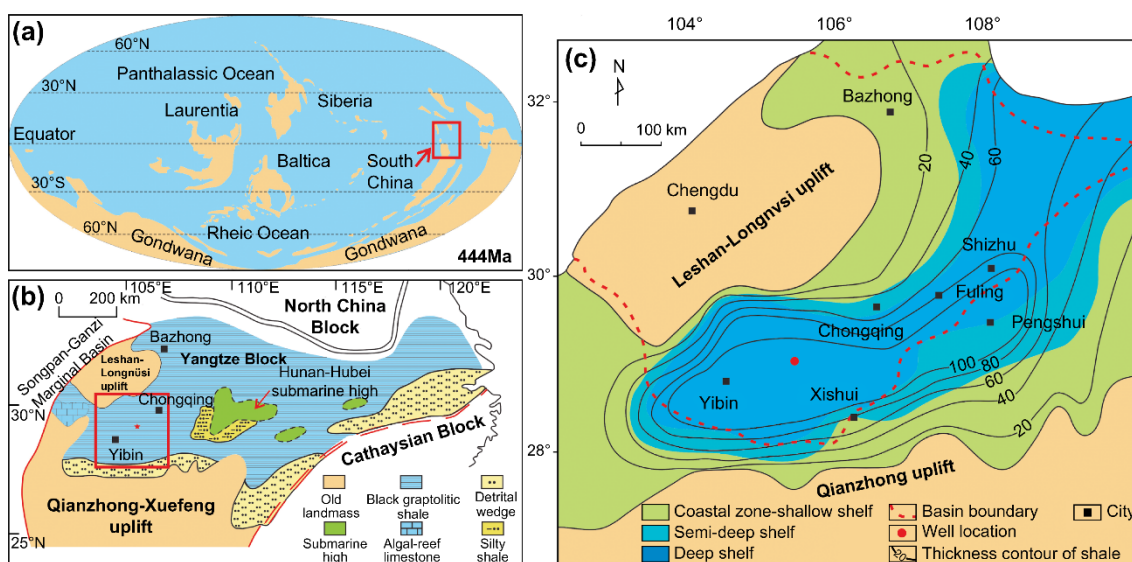


Figure 1. (a) A brief overview of worldwide paleogeography about 444 Ma. The red box in indicates the area that is shown in more detail in (b) (modified from <https://deeptimemaps.com>, accessed on 15 June 2023). (b) Paleogeographic map of the Yangtze Sea shelf about 444 Ma, specifically highlighting the geographical positioning of the south part of Sichuan Basin. The red box indicates the area that is further shown in (c) (modified from [18]). (c) Paleogeographic map of the south part of Sichuan Basin and its adjacent regions, including the well location (modified from [18]).

The fine-grained sequence (up to 522 m thick) is mainly distributed in the Wufeng–Longmaxi Formations in the southern Sichuan Basin (Figure 2). The shale stratum consists of the Wufeng, Guanyinqiao, and Longmaxi formations, from deep to shallow depths. The Wufeng Formation is comprised predominantly of blackish-gray shale containing carbon, silicon, and mudstone. It contains rich and diverse graptolitic fauna and radiolarians. The overlying Guanyinqiao Formation consists of limestone. The Longmaxi Formation exceeds the other two stratigraphic units in thickness. The lithology varies from black to graptolite-rich to carbonaceous shale, siliceous shale, carbonaceous mudstone, and gray-green mudstone. The Wufeng–Longmaxi Formation has a notable abundance of trace elements, such as manganese (Mn), uranium (U), nickel (Ni), and rare earth elements (REEs) [16,17]. These elements may be used to extract valuable insights on the enrichment process of organic matter (OM) and the origins of sediment.

The purpose of this study was to infer the provenance and tectonic background of the shale of the Wufeng–Longmaxi Formation on the Yangtze River Platform by evaluating the changes in weathering, sorting, and recycling processes based on analyses of mineralogical and geochemical characteristics. This study classifies six blocks of OM enrichment and explains their influencing factors, and it is expected to serve as a reference for other shales of the same age worldwide.

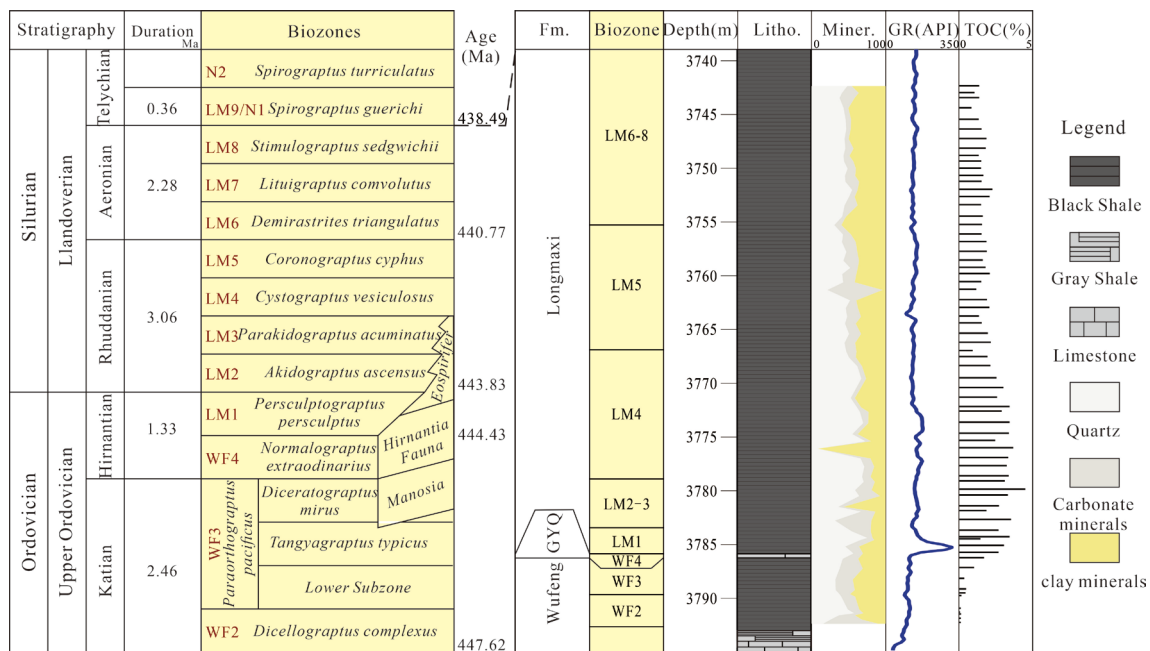


Figure 2. Graptolite biostratigraphy, lithofacies profiles, mineral compositions, gamma curve, and TOC content profiles of Wufeng–Longmaxi Formation located in the south Sichuan Basin (modified from [30,34–36]).

3. Materials and Methods

A total of 69 samples of black shale were taken from borehole YH for the purpose of this investigation. The southern Sichuan Basin yielded black shales from the Wufeng, Guanyinqiao, and Longmaxi formations, which exhibited a notable abundance of organic matter (Figure 3). We selected samples from all formations from the base to the top to ensure that they were representative. Ten large cores measuring 7 × 5 cm were prepared by sectioning bottom-up and perpendicular to the surface of the shale lamination. Ten slices measuring 5 cm × 7 cm × 30 μm were collected near the site for the macroscopic description of stratifications (Figure 3). Twenty samples, each measuring 2 cm × 2 cm × 20 μm and exhibiting distinct mineralogical compositions, were examined using scanning electron microscopy (SEM) to determine the lithological characteristics. All samples were analyzed for TOC and subjected to X-ray diffraction (XRD), X-ray fluorescence (XRF), and inductively coupled plasma mass spectrometry (ICP-MS) to investigate the relationship between OM accumulation, its provenance, and the paleoenvironment. All experiments were conducted at the National Energy Shale Gas R&D (Experimental) Center in China.

3.1. Lamination Analysis

Large-scale observations using a polarization microscope and panoramic photography were used to describe lamina. A miniature high-precision digital platform (Leica DM4500 P, Leica, Wetzlar, Germany) was used for large-area sectional photography. Features of lamina were visualized using panoramic photography. The petrographic properties of the standard thin sections were examined using a polarization microscope (DMIP, Leica) with a DFC450 photo system.

3.2. Mineral Composition and Morphological Analysis

Powder samples were analyzed using XRD. The samples were pulverized to –200 mesh and dried at 50 °C for 5 h. The scanning range of the diffraction pattern was 5–90°, the hole diameter was 1 mm, and the scanning speed was 4°/min. The experiment was performed using an X-ray diffractometer (PANalysis X-Pert PRO MPD, Amsterdam, The Netherlands). The operating voltage was 50 keV, and the current was 800 A. Sample preparation and

spectral identification abide by the China Petroleum and Natural Gas Industry Standard (SY/T5163-2014). Quantitative analysis of the mineral content was performed according to Chinese regulations (SY/T 5163-2010).

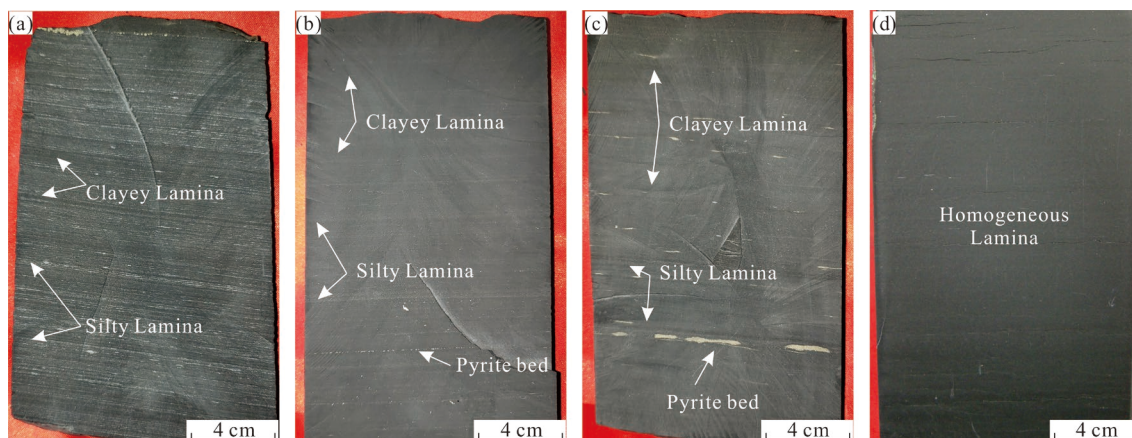


Figure 3. Photographs of cores showing the general characteristics of the samples from borehole YH. (a) Alternation between silty and clayey lamina, 3755.28 m, LM5. (b,c) The color of adjacent layers shows subtle differences as well as intermittent bright pyrite beds (Sample b from 3779.13 m, LM2–3; Sample c from 3785.13 m, LM1). (d) The shale is homogeneous, without obvious lamination, bedding, or fission, 3789.8 m, WF2.

Field-emission scanning electron microscopy (FE-SEM) and energy-dispersive X-ray spectrometry (EDS, New York, NY, USA) were used to measure the morphology of the minerals/organics, study the properties of the fracture, and determine the composition of the filling. Selected samples with different mineral compositions were cut into $8\text{ mm} \times 6\text{ mm} \times 2\text{ mm}$ slices and then polished to a thickness of 0.1 mm using Ar ions at 4 kV and an angle of 7.5° for 2 h using a 600 Duo Mill (Gatan, New York, NY, USA). The dimensions of the polished surface were $1500\text{ }\mu\text{m} \times 500\text{ }\mu\text{m}$, and it was semi-elliptical in shape. The thickness of the Pt coating was 20 nm.

3.3. Geochemical Analysis

The TOC value was quantified by immersing the samples in a solution of 4 M hydrochloric acid (HCl) at a temperature of $60\text{ }^\circ\text{C}$ for a duration of at least 24 h. Thereafter, distilled water was used to rinse away impurities and HCl, and the mixture was dried for two days. A LECO CS-400 analyzer (LECO, New York, NY, USA) was used for the analysis, and the observed standard deviation was found to be below 0.10%.

The samples' major element concentrations were measured using an XRF-1500 spectrometer (Thermo Fisher, New York, NY, USA). Samples were pulverized to -200 mesh in an onyx mortar, dried, and weighed to exactly 1.2 g. Samples were then thoroughly mixed with 6 g of lithium tetraborate ($\text{Li}_2\text{B}_4\text{O}_7$) in a mixing container. The combined material was transferred to a platinum crucible and heated to $1100\text{ }^\circ\text{C}$ to create a glass slide. The accuracy of the primary elemental analysis was $\pm 3\%$.

Trace element concentrations were quantified using ICP-MS (AMETEK, Berlin, Germany). Evenly comminuted samples with a precise weight of 100 mg were placed into a tightly closed Teflon beaker and digested using 0.5 mL HNO_3 , 2.5 mL HF, and 0.5 mL HClO_4 . Following this, an additional digestion was carried out with 1 mL HNO_3 and 3 mL H_2O . We then analyzed a 1:1000 dilution of the bulk solution using a VG PQ2 Fast ICP-MS. The accuracy of elemental analysis exceeded 4%. Standard OU-6 (shale), AMH-1 (andesite), and GBPG-1 (orthopyroxene) samples were used for monitoring. Trace elements were analyzed with an accuracy of $>0.5\%$. A comparative assessment was conducted between the estimated concentrations of major and trace elements in the studied shales and those

present in the Post-Archean Australian Shales (PAAS) and Phanerozoic North American Shale Composite (NASC) [24,37].

The effective indices for predicting the material composition and chemical weathering intensity of the clastic sedimentary source area are the chemical index of alteration (CIA) and the index of compositional variability (ICV) [38]. The formula for CIA is as follows: $CIA = Al_2O_3 / [(Al_2O_3 + CaO^* + Na_2O + K_2O)] \times 100$. The main components of the formula are expressed in terms of mole fractions. McLennan et al. established the following rule: $m(CaO^*) = m(Na_2O)$ when the mole fraction of CaO is larger than that of Na₂O; otherwise, $m(CaO^*) = m(CaO)$ [39]. As studies progress, the CIA value also has a corresponding indicative value for the paleoclimate [40,41]. A CIA value < 60 reflects low chemical weathering intensity and cold and dry climatic conditions. A CIA achievement ranging from 60 to 80 indicates the presence of mild weathering caused by chemicals and a humid and warmer environment. When the CIA value ranges from 80 to 100, it signifies a significant degree of chemical weathering and a climate characterized by higher temperatures and humidity.

The ICV is extensively utilized as an indicator of ascertaining whether the composition of source rock is the first-deposited sediment or recycled sediment. The calculation formula is $ICV = (Fe_2O_{3T} + K_2O + Na_2O + CaO^* + MgO + MnO + TiO_2) / Al_2O_3$. All components in the formula are expressed as mole fractions, and CaO* denotes CaO present in silicate rocks. When the ICV > 1, it suggests that sediments with a limited presence of clay minerals have a low level of compositional maturity. This implies that those sediments initially developed in accordance with geological structured movement. An ICV < 1 indicates that the compositional maturity of the clastic rocks is high, and that they contain a large quantity of clay minerals. Sedimentary materials undergo recycling or initial deposition under strong chemical weathering conditions, which are strongly influenced by epigenetic effects [42,43].

4. Results

4.1. Lithology and Lamination

Lithologically, the Wufeng–Longmaxi Formation in the south of the Sichuan Basin is composed mostly of siliceous, calcareous, and mixed shales. Various combinations of clay and silty lamina exist in the bedding. In the core photos, the homogeneous bedding of the lower Wufeng Formation (Figure 3d) to the upper Longmaxi Formation has increasingly dense sand-mud laminated interbeds (Figure 3a–c). Pyrite beds can be observed in the silty lamination (Figure 3b,c).

Five different types of beddings from deep to shallow depths are found in the following order: homogeneous bedding (Figures 3d and 4a), graded horizontal bedding (Figure 4b), banded silty sand horizontal bedding (Figure 4c,d), sand-mud-graded horizontal bedding (Figure 4d,e), and sand-mud thin interbedded horizontal bedding (Figure 4f) [28,44]. The first two types are prevalent in the Wufeng Formation (Figure 4a,b), whereas the others are ubiquitous in the Longmaxi Formation (Figure 4c,f).

In the WF2 member, the homogeneous bedding contains a large amount of bioturbation (Figure 4a). In WF3, clay lamina shows a positively graded horizontal laminaset (Figure 4b). In LM1, the banded silty sand horizontal bedding in a calcareous shale phase gradually transitions to a siliceous shale phase (Figure 4c). In LM2–3, sandy mud horizontal beddings present a small laminaset of silty lamina (Figure 4d,f). In LM4, graded bedding is composed of siltstone and claystone (Figure 4d,e). In LM6–8, silty and clay lamina are interbedded (Figure 4e,f).

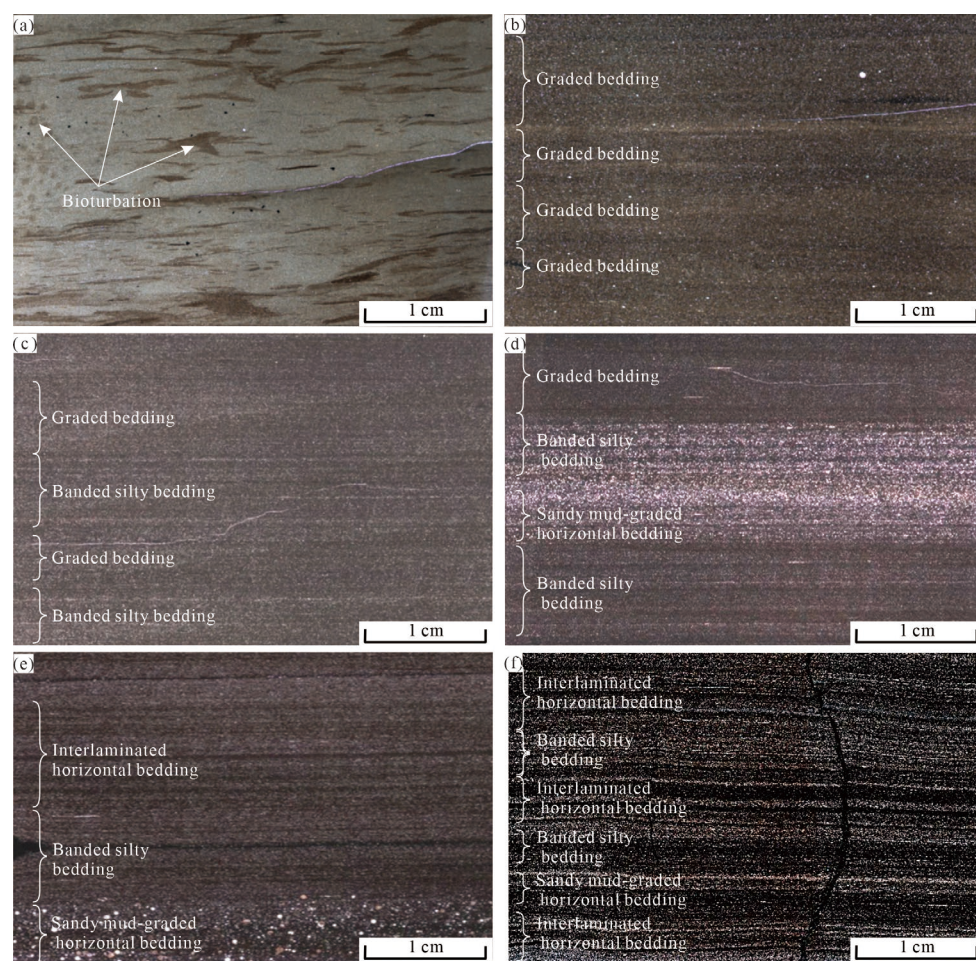


Figure 4. Photographs showing typical lamina, stratigraphy, and bedding in the Wufeng–Longmaxi Formation located in the southern region of the Sichuan Basin, China. (a) Bioturbated-type homogeneous beddings, 3789.8 m, WF2. (b) Graded beddings composed of claystone, 3787.19 m, WF3. (c) Banded silty bedding shale, 3783.72 m, LM1. (d) Sandy mud-graded horizontal bedding, 3780.45 m, LM2–3. (e) Lower part represents sandy mud-graded horizontal bedding, middle part shows banded silty bedding, and upper part features interlaminated horizontal bedding, 3768.41 m, LM4. (f) Interbedded silt lamina and mud lamina, 3754.5 m, LM6–8.

4.2. Organic Matter Distribution and Mineral Compositions

TOC and quartz contents gradually decreased, whereas the clay mineral and carbonate contents increased. The TOC content exhibited a wide range, spanning from 0.05% to 4.52%, with a mean value of 1.91%. The TOC value changed with depth: 3785.78–3767.01 m at 0.92%–4.52% in LM1–4 (abbreviation for LM1 to LM4), 2.89% on average. The average total organic carbon (TOC) contents of the other layers were as follows: WF4: 1.79%, LM5: 1.72%, and LM6–8: 1.53%. In contrast, WF3 has a significantly lower average TOC of 0.56%, and WF2 has the lowest average TOC of only 0.1%. Previous research suggests that the majority of kerogen samples display typical sapropelic kerogen properties, with an initial hydrogen index range of 650–950 mg/g (average, 800 mg/g) [45]. The Wufeng–Longmaxi Formation shale located in the southern region of Sichuan is often characterized by being at an advanced stage of maturation. The average maturity of OM is approximately 3.14% [46]. According to the occurrence conditions, genesis, and source of OM, the sample OM was classified into tangible OM and amorphous OM (AOM) [47]. The samples dominated by AOM were distributed around quartz, carbonate minerals, and pyrite grains. Additionally, there were small amounts of OM mixed with clay minerals, resulting in the formation of organomineral aggregates (Figure 5a,b,h).

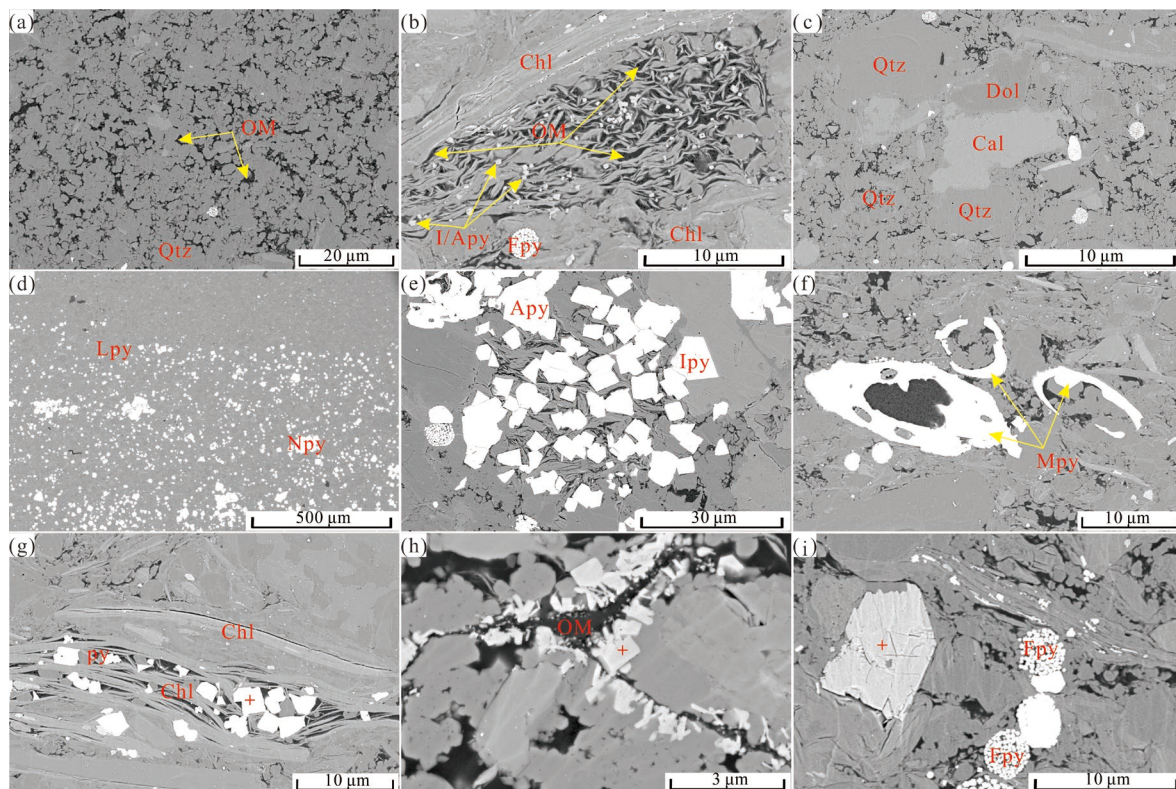


Figure 5. The characteristic mineral composition of the Wufeng–Longmaxi shale located in the southern Sichuan Basin, China, using scanning electron microscopy. (a) Siliceous shale primarily consisted of biological remains converted into quartz (Qtz), organic matter (OM), and other minerals. (b) OM was mixed with clay minerals or authigenic Qtz, and flaky or pinnate clay minerals were observed in the automorphic structure partially symbiotic with pyrite (Py), 3766.23 m, LM5. (c), Calcite, dolomite particles, external irregular, 3781.9 m, LM2–3. (d) Laminar (L)/nodular (N) Py enriched to a certain extent presented fine banded and thin laminated bedding, 3788.2 m, WF3. (e) Idiomorphic (I) Py aggregates were often found near or at the edge of OM and framboidal (F) Py aggregates. Allotriomorphic (A) Py aggregates were usually irregular monomer particles or irregular aggregate masses, 3782.72 m, LM2–3. (f) Radiolarian filled with Py, 3776.05 m, LM4. (g) Banded chlorite (Chl) with I/APy, pyrite represented by red cross, 3766.23 m, LM5. (h) Apatite, represented by red cross, 3782.72 m, LM2–3. (i) Rutile, represented by red cross, 3783.72 m, LM1.

The mineral components of the organic shale from the Wufeng–Longmaxi Formation are shown in Table S1. The predominant mineral composition consisted of quartz, clay minerals, and calcite, accompanied by minor amounts of dolomite, feldspar, pyrite, apatite, and rutile (Figures 5 and 6).

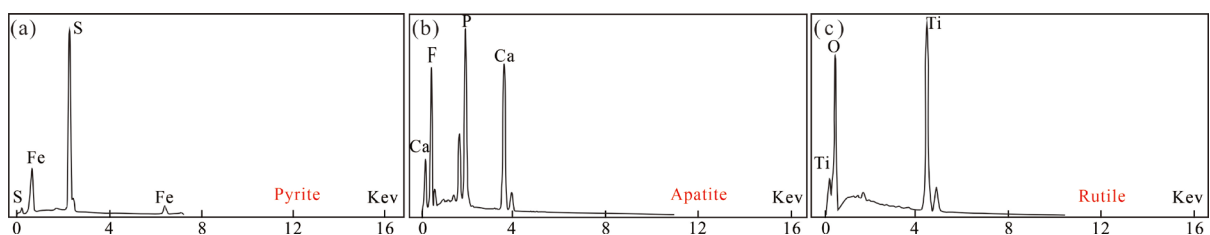


Figure 6. EDS spectra of pyrite, apatite, and rutile. (a) EDS spectrum of pyrite from Sample 44, 3776.05 m, LM4. (b) EDS spectrum of apatite from Sample 53, 3782.72 m, LM2–3. (c) EDS spectrum of rutile from Sample 54, 3783.72 m, LM1.

The quartz content of the Wufeng–Longmaxi Formation in southern Sichuan varies greatly, from 6.91% to 71.76% (average, 43.94%). As shown in Figure 2, during the initial WF2 stage, the quartz content was relatively low, averaging 43.94%. This was further reduced to its lowest point during the WF3 period, reaching a minimum of 32.25%. However, as the WF4 stage commenced, the quartz content gradually increased and eventually reached an average of 39.38%. In the subsequent LM1–4 period, the quartz content continued to increase, peaking at a maximum of 53.76%. Nevertheless, during the ensuing LM5 phase, the quartz content experienced a slight fluctuation, decreasing to 36.77%. Ultimately, during the LM6–8 period, the quartz content stabilized, maintaining an average of approximately 41.39%. Black shale quartz includes four main categories: terrestrial detrital quartz, biogenic quartz, secondary enlargement quartz, and clay mineral transformation quartz. The terrestrial quartz content was low, with angular or sub-angular micro-particles (10–20 μm); the closer it was to the source area, the greater the content. Under the microscope, bio-quartz was enriched with radiolarians and siliceous sponge bone needles. Moreover, the presence of biogenic silica can be inferred, because the quartz crystallinity index (QCI) values were <8 in LM1–4 and WF2–3 [48]. The secondary enlargement of quartz at the periphery of the cathode luminescence image did not glow. The clay mineral-transformed quartz was distributed around or encased in the illite minerals.

The range of carbonate mineral concentration observed in the samples varied from 4.72% to 72.61%, with an average value of 15.43%. The majority of carbonate minerals were calcite and dolomite. Both were interspersed between other mineral particles of great size, generally 10–20 μm (Figure 5c). Upon examination from bottom to top, the carbonate mineral content in the Wufeng Formation is evidently higher than that in the Longmaxi Formation (Figure 2). Within the Wufeng Formation, the carbonate mineral content gradually decreases, with average contents of 29.6%, 22.52%, and 20.15% for WF2, WF3, and WF4, respectively. In contrast, the Longmaxi Formation exhibits an average carbonate mineral content of 13.41% for LM1–4 and 16.76% for LM5, and it further decreases to an average of 10.26% for LM6–8. These data reveal a distinct variation and trend in carbonate mineral content from the Wufeng to the Longmaxi Formations. The range of calcite content observed in the samples varied from 0.74% to 72.17%, with an average value of 7.48%. Under SEM, an irregular shape with a relatively light hue was observed, with dissolution pores, longitudinal stripes, and crush marks on the surface. The clay minerals converged around the particles. The dolomite content ranged from 0.44% to 40.63%, with a mean of 7.94%. Under SEM, the dolomite particles were dark, mostly showing regularly shaped crystals. In black shale, carbonate minerals can be divided into terrigenous, biogenic, primary chemical precipitation, and diagenetic transformation origins, according to their sources. Calcite is an irregular particle shape, and dissolution pores can be observed on the surface, indicating its terrestrial origin. The dolomite minerals are in close proximity to the surrounding minerals and are formed in a contiguous manner. It is speculated that dolomite minerals are formed by the diagenetic transformation of calcite. In the deep-water shelf sedimentary environment, the dilution effect of terrigenous clastics is minimal, whereas the content and distribution of carbonate minerals are mainly controlled by water depth and distance from terrigenous sources. The higher the water depth and the greater the distance from terrigenous sources, the lower the content of carbonate minerals. The lower the water depth and the smaller the distance from terrigenous sources, the higher the content of carbonate minerals [49].

The clay mineral content was 4.04%–81.39% (average, 32.32%). The overall trend of clay mineral content followed an initial increase, followed by a subsequent decrease (Figure 2). The average clay mineral content during the WF2 stage was 30.37%, increasing to 38.81% during the WF3 stage and further increasing to 35.41% during the WF4 stage. However, the clay mineral content decreased to 22.63% during the LM1–4 stages and increased to 32.9% during the LM5 stage. Finally, it reached 40.45% during the LM6–8 stages. This trend reflects the variability in clay mineral content during the different stages. The predominant clay minerals identified in the samples were illite, chlorite, a mixed layer of illite and smectite

(I/S), and kaolinite. Illite was usually a flaky, needle-like, or flaky aggregate, and there were traces of weathering and transport on larger particle-sized debris. Chlorite was mostly long striped, often curved, or deformed in the shape of debris particles. The I/S mixed layers were mostly scaly, and the aggregates were honeycombed. Quartz and pyrite particles were embedded or encased in the minerals (Figure 5b,g,i). Most of the clay minerals originate from the weathered products of the parent rock and are mechanically deposited. The formation of clay minerals is governed by the source, whereby areas in proximity to the source exhibit a higher clay mineral content [49]. The diagenetic evolution sequence of clay minerals typically follows the conversion of montmorillonite into illite-smectite mixed layers, which is then transformed into illite [50]. The shale in the study area has undergone high-over mature evolution, resulting in the complete transformation of primary montmorillonite into illite or illite-montmorillonite mixed layers [51]. Additionally, the needle-shaped secondary illite minerals are predominantly enclosed by micron-submicron quartz particles.

The pyrite concentration varied from 0.42% to 10.14%, with a mean of 2.07%. Four main types of pyrites were present in the studied formation: lamina (nodular) pyrite (I/NPy), idiomorphic (allotriomorphic) pyrite (I/APy), FPy pyrite (framboidal), and metasomatic pyrite (MPy). L/NPy was normally a cubic self-formed crystal that was enriched to some extent, showing a macroscopically finely banded thin lamination and NPy generated along the lamination (Figure 5d). In the early diagenesis process, the loose sediments have large pores and good connectivity, facilitating the growth and aggregation of pyrite crystallites within the pores, resulting in the formation of agglomerated pyrite. After diagenesis, the pore space becomes smaller, and the pyrite crystallites continue to grow and aggregate, resulting in the formation of lamellar and nodular pyrite. Pyrite is formed by the polymerization of FeS_2 , resulting from the reaction between sulfur and FeS, with the latter being formed by bacterial sulfate reduction and thermochemical sulfate reduction. The presence of I/NPy suggests a transition of the sedimentary environment towards an acidic, sulfidic-reducing condition favorable for organic matter preservation and enrichment [52]. This is also confirmed by the pyrite bed in the LM1 core of the organic-rich section in Figure 3c. IPy usually coexisted with clay particles or lamellar crystals or existed around OM and FPy aggregates. Compared to FPy crystals and aggregates, the APy crystals and aggregates were usually irregular single particles or irregular clumps (Figure 5b,e). FPy had a strawberry structure (Figure 5b,i). MPy refers to the pyrite substitute for sponge needles and radiolarians (Figure 5f). Some MPy was distributed in the strips near the OM, and they filled the fractures near the OM.

Based on the findings of this research, the predominant types of pyrite found within the shale reservoirs of the Wufeng–Longmaxi Formation located in the Sichuan Basin were FPy and its aggregates, which are linked to OM. Wufeng–Longmaxi shale is a marine shale abundant in OM, and it is formed under a favorable reducing environment with Fe and S elements, low temperature, and organic richness, resulting in significant FPy formation [53–60]. The finding is consistent with a sulfur-rich sedimentary environment, as indicated by the S/Fe atomic number ratio ranging from 1.8 to 2.1 in pyrite samples [61].

Among them, the organic matter enrichment section LM1–4 widely develops banded silt-type horizontal bedding and sand-mud-graded horizontal bedding, which exhibits the characteristics of high TOC and high quartz. In comparison, the quartz content of the shale in the Wufeng Formation is substantially lower than that in the Longmaxi Formation, averaging 34.4%. This could be attributed to the melting of the Gondwana Glacier, gradual climate warming, sea level rise, the evolution of a large number of graptolites adapted to the new environment, and organic matter enrichment [35,44].

4.3. Major Elements

The oxide content of the main elements from the Wufeng–Longmaxi shale is consistent with the mineral composition, which was mainly comprised of quartz, clay, calcite, and dolomite (Table S2). XRF showed that the main oxides were SiO_2 and Al_2O_3 at

36.01%–72.65% (average, 59.09%) and 6.24%–20.04% (average, 12.58%), respectively. In comparison, the lower-grade oxides were CaO, Fe₂O_{3T} (the total content of Fe₂O₃ and FeO), K₂O, and MgO, with averages of 5.09% (1.18%–18.53%), 5.09% (1.91%–26.46%), 3.05% (1.41%–4.78%), and 2.64% (1.33%–4.43%), respectively. Other oxides such as MnO, Na₂O, P₂O₅, and TiO₂ were below 1.0%. The average contents of the major elements significantly differed in comparison with PAAS and NAAS contents. The only component that was more than five times greater than PAAS and NAAS was CaO. This shows that the carbonate mineral content is high. All other contents were much lower. The contents of Fe₂O_{3T} and TiO₂ were less than half those of PAAS and NAAS.

4.4. Trace Elements

Table S3 provides the analytical data for REE. Figure 7 illustrates the chondrite-normalized model. The calculation of Eu anomalies was performed in the following manner: $Eu/Eu^* = (Eu_N) / [(Sm_N \times Gd_N) / 2]$, where subscript N represents the REE normalized to the chondrite value [26]. The REE distribution curves of all samples exhibit comparable patterns, characterized by a minor enrichment of light REEs (LREEs), generally lower concentrations of heavy REEs. It is accompanied by the trend of Eu negative anomaly distribution (Figure 7).

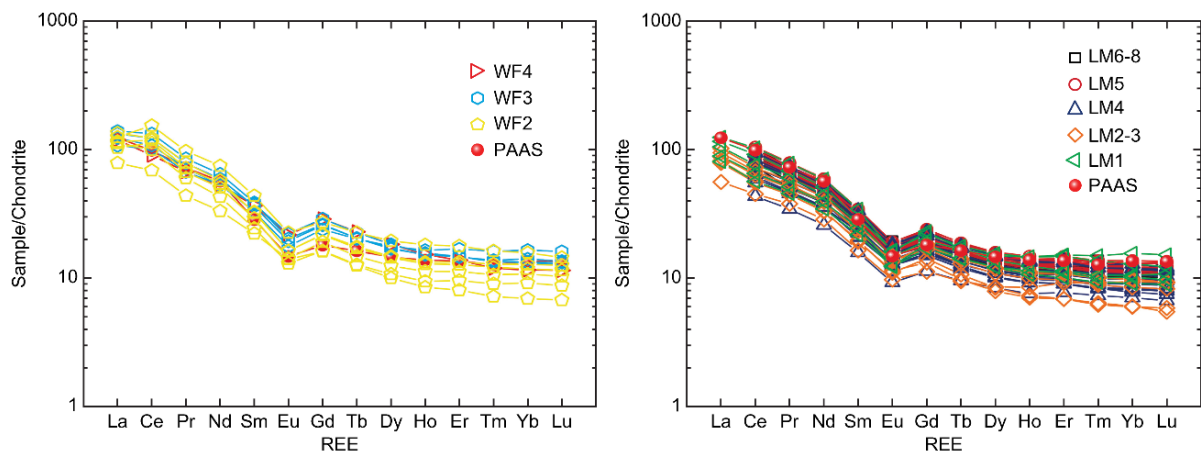


Figure 7. Rare earth element (REE) standardized patterns of globular meteorites from shale sedimentary rocks of the Wufeng–Longmaxi Formation, southern Sichuan Basin.

The Σ REE (the total REE content) showed significant variability (84.67–253.49 ppm; average, 161.02 ppm), which was lower than that of PAAS (184.77 ppm [26]) and higher than that of NASC (140.56 ppm [39]). The Σ REE content of the Wufeng Formation ranged from 167.19 to 253.49 μ g/g, with an average of 202.55 μ g/g ($n = 11$). In the Longmaxi Formation, the Σ REE content ranged from 84.67 to 199.18 μ g/g, with an average of 154.42 μ g/g ($n = 58$). For LM1–4, the Σ REE content ranged from 84.67 to 191.25 μ g/g, with an average of 136.53 μ g/g ($n = 26$). LM5–8 (abbreviation for LM5 to LM6–8) exhibited a Σ REE content ranging from 132.24 to 199.18 μ g/g, with an average of 168.97 μ g/g ($n = 32$). The difference between the average Σ REE values of the upper and lower sections of the Longmaxi Formation and differences between the Wufeng Formation and the Longmaxi Formation are significantly greater than the difference between the average Σ REE values of the entire Longmaxi Formation and the North American shale, indicating variations in the geochemical conditions of shale during different periods in the area.

The concentration of Σ LREE (74.57–229.8 ppm; average, 145.67 ppm) was on average 8.86 times higher than that of Σ HREE (heavy REEs, 9.96–23.69 ppm; average, 16.43 ppm). The L/H(Σ LREE/ Σ HREE) value was between 6.87 and 11.47, with an average of 8.86 (Table S3). The average L/H value of LM5–8 was 9; for LM1–4, it was 8.44; and for WF2–3, it was 9.49. The degree of differentiation of light and heavy rare earth elements was highly similar, indicating that the provenance of shale in the area remains unaltered. The La–Eu

segment had an evident right trend with a steep gradient, whereas the Gd–Lu segment was flat with a low angle and a negative Eu anomaly (Eu/Eu^* values 0.57–0.79; average, 0.68), showing LREE enrichment (Figure 7). The total fractionation index (La_N/Yb_N) of REE was 5.94–13.63 (average, 9.79). The above L/H and La_N/Yb_N values show that the provenance of the shale in the Wufeng–Longmaxi Formation in southern Sichuan has not undergone marked changes, which could serve as a basis for identifying the provenance and distinguishing the tectonic background.

5. Discussion

5.1. Sedimentary Sorting and Recycling

The preferential accumulation of heavy minerals in clastic sedimentary rocks results in deviations in the distribution of some chemical components, thereby complicating the interpretation of provenance [62]. Hydrodynamic sorting enriches heavy minerals, such as zircon, sphene, allanite, and apatite, and migrates some elements [63,64]. Similarly, REE and Th abundances may be contingent on the accumulation of these minerals. Major and trace elements play significant roles in identifying the accumulation of heavy minerals during sediment transport [44,65–67]. The ternary diagram of the Al_2O_3 – TiO_2 –Zr covariation demonstrates that the effect of weathering on the absolute contents of Al, Ti, and Zr was eliminated, thereby emphasizing the effect of the separation process. The limited TiO_2 and Zr fluctuation ranges deviated from the Zr– TiO_2 line, removing Ti and Al fractionation on Zr [65]; Figure 8a). The bivariate diagrams exhibited a weak and unsystematic association (Figure 8b–d), namely, the La/Sm vs. Th, Tb/Yb vs. Hf, and Ta/La vs. Ti plots, suggesting that heavy mineral accumulation might not have significant effects on the geochemical characteristics of sedimentary rocks in the surveyed region [66]. The aggregation of sphene and zircon can significantly increase the abundance of Th and Hf and fractionate the Ta/La ratios of sedimentary rocks, whereas that of apatite increases the La/Sm and Ta/La ratios and allanite Tb/Yb and Ta/La fractional ratios [66]. The accumulation of these heavy minerals was counter-indicated by the weak fractionation of the La/Sm, Ta/La, and Tb/Yb ratios (Figure 8b–d). These observations indicated that sedimentary sorting had little effect on the geochemical characteristics of these sedimentary rocks.

Sc and Th are quantitatively transported from source rocks to sediments, and their ratios reveal the composition of the sediment source [24]. During sediment recycling, minerals with low corrosion resistance are primarily eliminated, whereas Zr is gradually enriched [39,68]. Th/Sc and Zr/Sc ratios and their bivariate plots can be used to estimate the rate of sediment recycling and changes in mineral composition [24,68–71]. During sedimentary recycling, the Th/Sc ratios did not fluctuate noticeably compared with the Zr/Sc ratios. Although there is a significant correlation between the Th/Sc ratio (1.04–3.16; average, 1.45) and Zr/Sc ratio (4.97–30.27; average, 13.24), the Zr/Sc ratio shows a slight upward trend, indicating that source rocks have experienced less or no sedimentary cycles [69].

It is evident from Figure 8 that the sedimentary sorting process has a limited impact on the source rocks of each sub-layer from WF2 to LM6–8. Furthermore, the source rocks have not undergone any significant recycling processes.

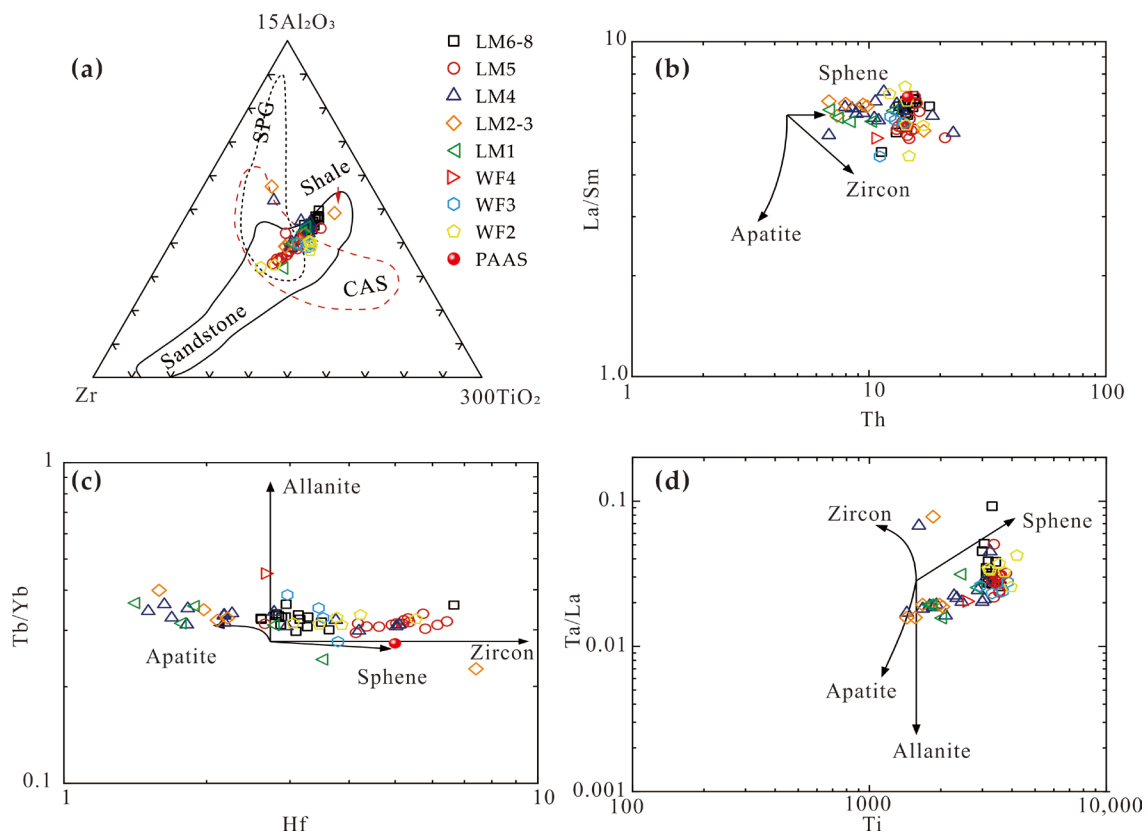


Figure 8. (a) Al_2O_3 - TiO_2 -Zr triangle diagram [65]. (b) La/Sm–Th bivariate diagram. (c) Tb/Yb–Hf bivariate diagram. (d) Ta/La–Ti bivariate diagram [66]. Demonstrating the impacts of sedimentation separation effect. Note. CAS = calc-alkaline suites. SPG = strongly peraluminous granites.

5.2. Paleoweathering and Paleoclimate

Under humid conditions, the chemical weathering of rocks is enhanced, the Al and Si contents increase, and alkali metals such as Na, K, and Ca are leached. The most commonly used index for evaluating the extent of chemical weathering is the CIA [38]. Weathering is strongly influenced by climate; pronounced chemical weathering prevails under warm and humid conditions, whereas weaker weathering is linked to cold and arid environments [72,73]. Overall, the CIA values exhibited a narrow range of variation, between 63.24 and 73.32, with an average value of 67.95. There was a gradually increasing trend in CIA from WF2 to LM6–8, with slight fluctuations. Specifically, a lower CIA value (64.97) was observed during LM5. Despite the occurrence of two interglacial periods during WF4, the limited number of samples in the present study precluded the observation of significantly low values in the overall mean. Based on the aforementioned patterns of the CIA values, the paleoweathering intensity and paleoclimate characteristics of the Wufeng Formation to the Longmaxi Formation generally exhibit a gradually increasing trend of moderate weathering under warm and humid conditions. Within this period, two distinct changes occurred, specifically during WF4 and LM5. An ICV–CIA correlation diagram was used to describe the geological history of the sediments and evaluate the strength of their chemical alteration (Figure 9a). The ICV values ranged between 1.04 and 2.23, exhibiting slight fluctuations but generally stabilizing at 1.35. Specifically, higher values were observed in WF3 and LM1–4, at 1.57 and 1.35, respectively. The remaining values for WF2, LM5, and LM6–8 were 1.26, 1.34, and 1.21, respectively. The source rocks are sediments that were deposited during a tectonically active period, representing the initial deposition in that particular geological setting.

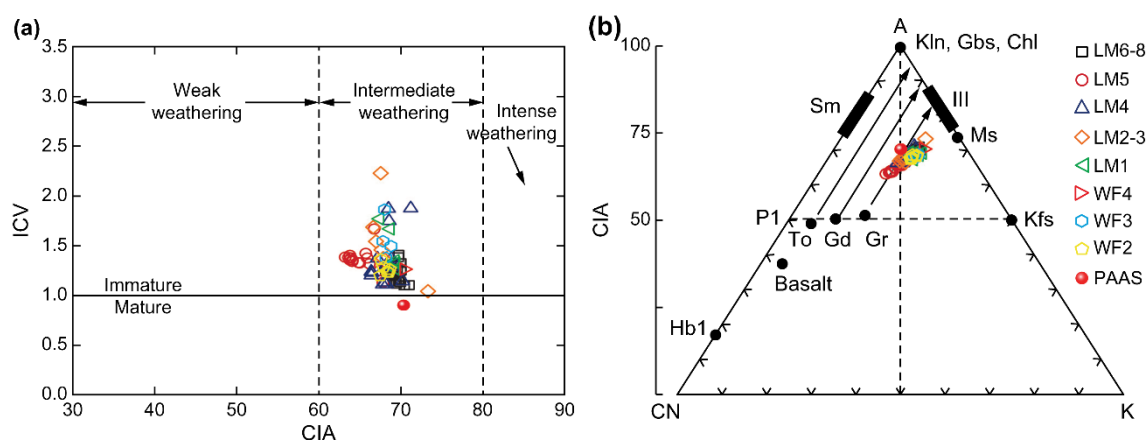


Figure 9. (a) ICV–CIA bivariate diagram. (b) A–CN–K triangle diagram showing the effect of paleoweathering and paleoclimate. Data for tonalite (To), granodiorite (Gd), granite (Gr), and post-Archean Australian shales (PAAS) were obtained from Taylor and McLennan [24]. Note: Chl: chlorite. Gbs: gibbsite. Hbl: hornblende. III: illite. Kfs: potassic feldspar. Kln: kaolinite. Ms: muscovite. Pl: plagioclase. Sm: smectite.

The A–CN–K (Al_2O_3 –($\text{CaO}^* + \text{Na}_2\text{O}$)– K_2O) ternary diagram is commonly used to quantify the degree of weathering and paleoclimate (Figure 9b [70–75]). Simultaneously, the CIA value is displayed in the A–CN–K triangle diagram to differentiate the component changes caused by weathering and the mineral content of source rocks [42,76]. Figure 9b shows that the samples were concentrated over the plagioclase–K-feldspar links and extended to a narrow linear trend of the A peak. The weathering trend line was almost parallel to the A–CN line, and there was no apparent tilt toward the K peak. This shows that K metasomatism had little effect on rocks during diagenesis. The point where the trend line extends downward and intersects the plagioclase–potash feldspar line is located near the granodiorite and granite (potential source rocks).

5.3. Provenance and Tectonic Setting

5.3.1. Provenance

The distribution patterns of REEs have crucial consequences for provenance analysis [77,78]. Owing to the lack of a strong association with major and trace elements, REEs exhibit stability subsequent to processes such as weathering, sorting, and modification and can be utilized to determine the origin of sedimentary rocks [77]. Acidic rocks often have high REEs and a clear negative Eu anomaly. Nevertheless, it is often observed that basic rocks generally exhibit a scarcity of REEs and lack a significant Eu anomaly or positive Eu anomaly [79]. All samples exhibited a moderately high concentration of REE (84.67–253.49 ppm; average, 160.98 ppm) and negative Eu anomalies, indicating that the provenance of the sediments may be linked to acidic igneous rocks. The characteristics of these sedimentary rocks, which are rich in LREE and depleted in HREE, support this conclusion.

The bivariate Th/Sc–Zr/Sc plot (Figure 10a) and ICV (>1) indicate immature components and sedimentary source rocks from the first cycle of deposits [39]. The A–CN–K diagram indicates that the protoliths of the samples were probably intermediate and acidic igneous rocks (Figure 9b). Similarly, the La/Th vs. Hf diagram shows that most samples are plotted in or near the felsic source field (Figure 10b). Based on the discriminant source map of the Al_2O_3 , TiO_2 , and Zr abundances, three attribute zones were distinguished: felsic, mafic, and intermediate igneous rocks [26]. The distribution of the shale samples shows that the provenance of the sediments was mainly derived from felsic igneous rocks (Figure 10c,d).

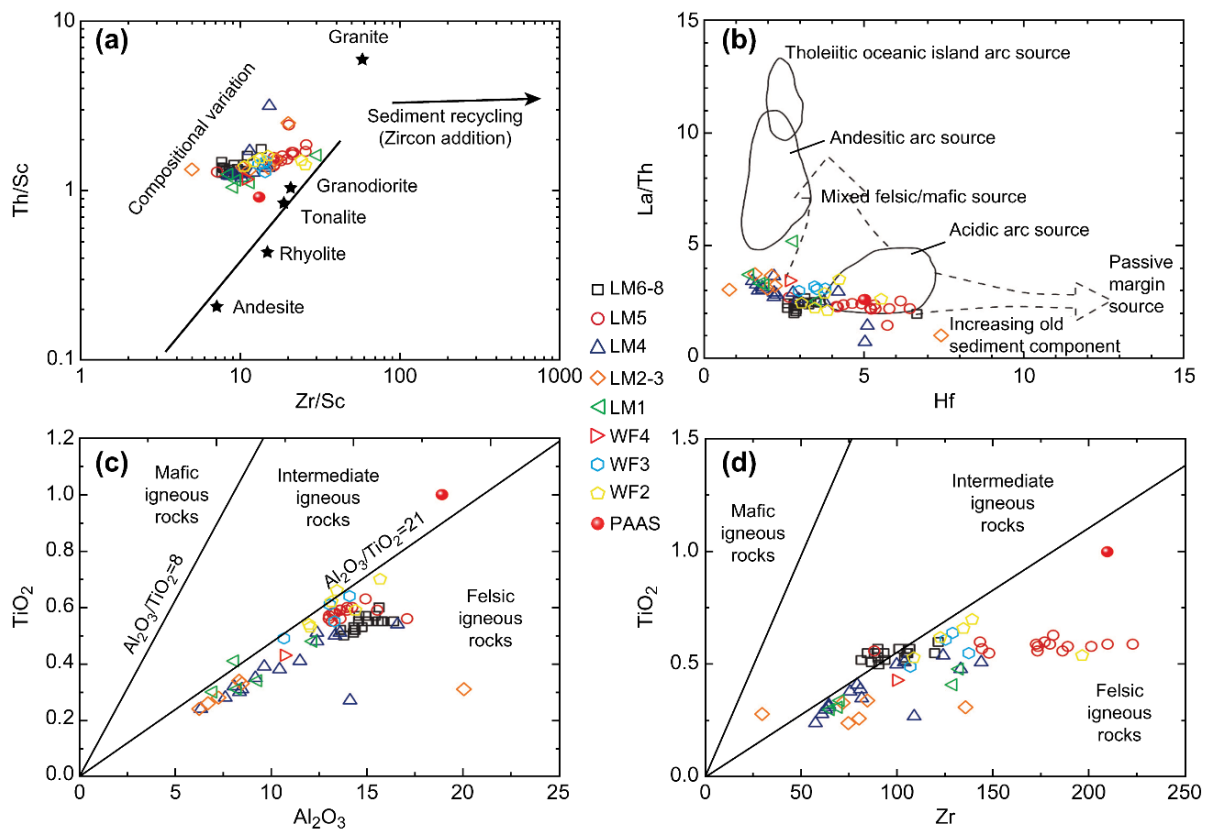


Figure 10. (a) Th/Sc–Zr/Sc discrimination graph for sedimentation recycling effect. (b) La/Th–Hf [80], (c) TiO₂–Al₂O₃ [27], and (d) TiO₂–Zr [27] diagrams for the discrimination of source compositions. The data regarding PAAS are derived from [24]. Note: PAAS = post-Archean Australian shales.

5.3.2. Tectonic Setting

Because the geochemistry properties of source rocks are considerably determined based on the tectonic environment of the source plate, the tectonic setting can be recognized by discriminant graphs based on element geochemistry [25,81–87]. The four tectonic settings of the continental island arc, oceanic island arc, active continental margin, and passive continental margin are characterized by TiO₂–Fe₂O_{3T} + MgO, K₂O + Na₂O–SiO₂, La–Th–Sc, and Th–Sc–Zr/10 (Figure 11 [25]). The majority of the samples were discovered inside or in close proximity to regions associated with the active continental margin and continental island arc (Figure 11a–d). Based on the discriminant function, major element diagrams of the clastic sediments were constructed under three main tectonic settings: arc (active volcanism), continental rift (extension), and continental collision (compression), where (SiO₂)_{adj} is the SiO₂ value obtained by fitting 10 principal elements to 100 wt% without volatility [85]. The structural discrimination of highly siliceous (SiO₂)_{adj} content ranging from 63% to 95% and low siliceous (SiO₂)_{adj} content ranging from 35% to 63% is effective for the identification of chemical changes associated with the analysis of weathering, recovery, and post-depositional processes [85]. All the analyzed shale samples were plotted in the collision field (continent to continent) on high-silica ($n = 52$) and low-silica ($n = 21$) multidimensional diagrams (Figure 11e,f).

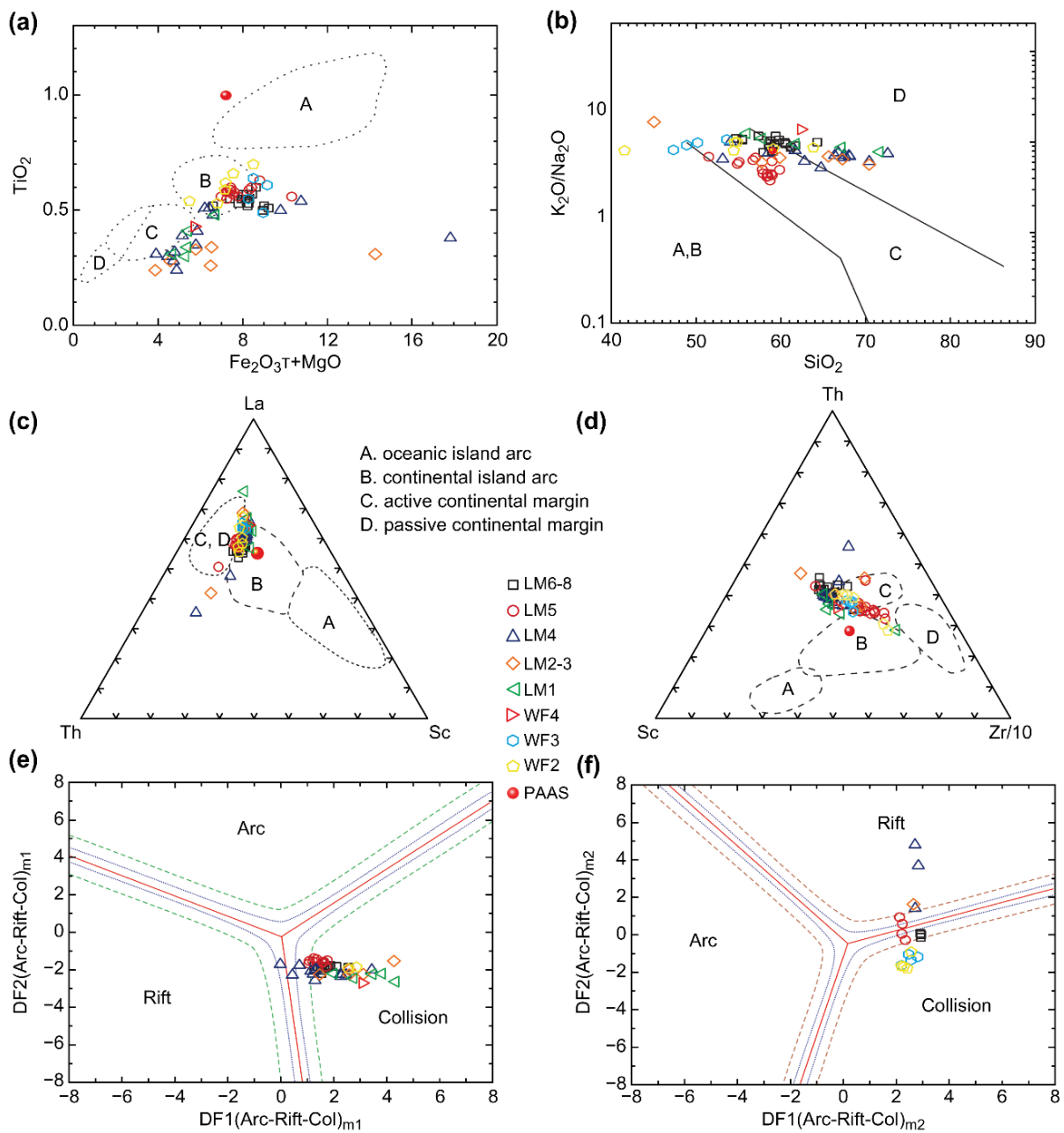


Figure 11. Discrimination diagrams for tectonic setting: (a) TiO₂–Fe₂O₃T + MgO [88]. (b) K₂O + Na₂O–SiO₂. (c) La–Th–Sc. (d) Th–Sc–Zr/10 [25]. (e) Discriminant function multidimensional mapping of high-silica clastic deposits in varied tectonic environments (arc, rift, and collision). (f) Discriminant function multidimensional mapping of low-silica clastic deposit in varied tectonic environments (arc, rift, and collision) [85].

High-silica type discriminant function equations:

$$DF1_{(Arc-Rift-Col)_{m1}} = (-0.263 \times \ln(TiO_2/SiO_2)_{adj}) + (0.604 \times \ln(Al_2O_3/SiO_2)_{adj}) + (-1.725 \times \ln(Fe_2O_3^t/SiO_2)_{adj}) + (0.660 \times \ln(MnO/SiO_2)_{adj}) + (2.191 \times \ln(MgO/SiO_2)_{adj}) + (0.144 \times \ln(CaO/SiO_2)_{adj}) + (-1.304 \times \ln(Na_2O/SiO_2)_{adj}) + (0.054 \times \ln(K_2O/SiO_2)_{adj}) + (-0.330 \times \ln(P_2O_5/SiO_2)_{adj}) + 1.588$$

$$DF2_{(Arc-Rift-Col)_{m1}} = (-1.196 \times \ln(TiO_2/SiO_2)_{adj}) + (1.604 \times \ln(Al_2O_3/SiO_2)_{adj}) + (0.303 \times \ln(Fe_2O_3^t/SiO_2)_{adj}) + (0.436 \times \ln(MnO/SiO_2)_{adj}) + (0.838 \times \ln(MgO/SiO_2)_{adj}) + (-0.407 \times \ln(CaO/SiO_2)_{adj}) + (1.021 \times \ln(Na_2O/SiO_2)_{adj}) + (-1.706 \times \ln(K_2O/SiO_2)_{adj}) + (-0.126 \times \ln(P_2O_5/SiO_2)_{adj}) - 1.068$$

Low-silica type discriminant function equations:

$$DF1_{(Arc-Rift-Col)m2} = (0.608 \times \ln(TiO_2/SiO_2)_{adj}) + (-1.854 \times \ln(Al_2O_3/SiO_2)_{adj}) + (0.299 \times \ln(Fe_2O_3^t/SiO_2)_{adj}) + (-0.550 \times \ln(MnO/SiO_2)_{adj}) + (0.120 \times \ln(MgO/SiO_2)_{adj}) + (0.194 \times \ln(CaO/SiO_2)_{adj}) + (-1.510 \times \ln(Na_2O/SiO_2)_{adj}) + (1.941 \times \ln(K_2O/SiO_2)_{adj}) + (0.003 \times \ln(P_2O_5/SiO_2)_{adj}) - 0.294$$

$$DF2_{(Arc-Rift-Col)m2} = (-0.554 \times \ln(TiO_2/SiO_2)_{adj}) + (-0.995 \times \ln(Al_2O_3/SiO_2)_{adj}) + (1.765 \times \ln(Fe_2O_3^t/SiO_2)_{adj}) + (-1.391 \times \ln(MnO/SiO_2)_{adj}) + (-1.034 \times \ln(MgO/SiO_2)_{adj}) + (0.225 \times \ln(CaO/SiO_2)_{adj}) + (0.713 \times \ln(Na_2O/SiO_2)_{adj}) + (0.330 \times \ln(K_2O/SiO_2)_{adj}) + (0.637 \times \ln(P_2O_5/SiO_2)_{adj}) - 3.631$$

5.4. Influences of Terrigenous Influx on OM Accumulation

The three main ways in which terrigenous inflow affects black shale rock composition and OM accumulation are as follows: as an adsorbent for organic aluminosilicate material, reducing the OM deposition rate and directly diluting the OM content, and governing the OM deposition rate and the effectiveness of bacterial decomposition [89–91].

Al is formed by chemical weathering linked to aluminosilicate clay minerals, whereas Ti is associated with clay and dense minerals like ilmenite and rutile [92–94]. A significant similarity exists between Al and Ti oxide contents, suggesting that Ti originates from detrimental aluminosilicates (Figure 12 [95,96]). The Σ REE for debris influx is significantly higher than the Σ REE for seawater, indicating that the relative sea level controls the input of debris influx and moves sediment overland (during the transgression) or into the basin (during the regression [97,98]). The sedimentation rates of LM1–5 were significantly lower than those of the other layers [34]. Owing to the restricted dilution of terrigenous influx, the reduced deposition rate was particularly beneficial for OM enrichment.

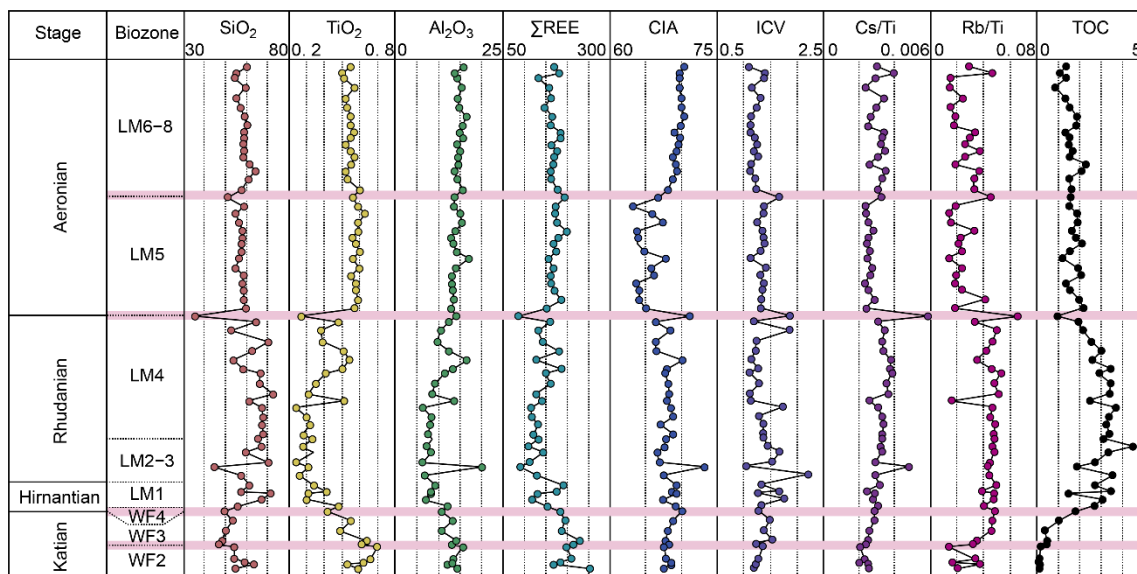


Figure 12. Variations in the contents of some major elements (%), total rare earth elements (ΣREE), chemical index of alteration (CIA), index of compositional variability (ICV), Ti-normalized ratios, and TOC contents (%) showing the changes in terrigenous influx and paleoclimate during the enrichment of OM.

Moreover, Rb and Cs are sensitive to climatic variations and can potentially undergo leaching because of chemical weathering processes [99]. Typically, an escalation in chemical weathering leads to elevated Rb and Cs concentrations. Consequently, the ratios of Cs/Ti and Rb/Ti serve as elemental proxies for reconstructing paleoclimate conditions [99,100].

The provenance parameter profile can be subdivided into six stages of OM-rich process according to the chemical stratigraphic study (Figure 12). For stage 1, which corresponds to biozone WF2, the stratification characteristics exhibit homogeneous bedding, and the rock type is siliceous shale. The mineral composition features low quartz, high calcium

carbonate, and high clay mineral contents. All the samples exhibited negligible or no OM enrichment (TOC average, 0.1%). Relatively high CIA (average, 68.09%), ICV (average, 1.26), Cs/Ti (average, 0.002), and Rb/Ti values (average, 0.026) indicate a relatively warm, semi-humid, and chemically persistent environment. The main elements in TiO_2 (average, 0.61%), Al_2O_3 (average, 13.43%), and ΣREE (average, 203.79%) indicate a comparatively high terrestrial input [101,102]. The low SiO_2 content suggests a deficiency in paleoproductivity, indicating a limited contribution of bio-quartz and lower organic matter content.

Stage 2 corresponds to the WF3 biozone and is characterized by gradual horizontal bedding of carbon-rich siliceous shales. This stage continues to be characterized by low quartz content, high carbonate mineral content, and high clay mineral content. The limited SiO_2 content suggests that it is in the early stage of organic matter accumulation. Concurrently, the TOC content sharply increased from 0.34% to 1.01% (average, 0.56%), and the corresponding terrestrial input parameters exhibited a clear downward trend over the same period (TiO_2 average, 0.57%; Al_2O_3 average, 12.77%; ΣREE average, 206.45%), indicating a decrease in terrestrial input. The paleoclimate of this period showed an increasing trend compared to that of Block 1 (Figure 12). Suitable environments and low terrestrial dilution are beneficial for OM accumulation.

For Stage 3, the biozones from WF4, the lithofacies is limestone. Compared to that of the WF3 period, mineral composition of this period showed an average increase of 7.1% in quartz content, a decrease of 2.4% in carbonate minerals, and a decrease of 3.4% in clay minerals. The increase in biogenic quartz indicated by previous analyses indicates enhancement in paleoproductivity, enabling organic matter accumulation to reach a remarkable level. Conversely, the overall decrease in terrestrial carbonate mineral and clay mineral content suggests a reduction in terrestrial input, creating conditions conducive to organic matter enrichment. This corroborates the average increase of 1.79% in TOC during this period. The abrupt change in lithofacies from black shale to limestone is related to the global sea level decline associated with the Hirnantian glaciation [102–108]. This alteration in lithology aligns with the timeline of glacial activity in numerous regions. Several studies have investigated the sedimentary features of this period and have observed that the reduction in sea level regulation resulted in the formation of limestone deposits, contributing to the widespread extinction of in situ graptolites [109]. In contrast, *Hirnantia sagittifera*, *Eostropheodonta parvicostellata* Rong, and other Hirnantian brachiopod fossils thrived and established a group of mesocrusts that were widespread regionally during the Hirnantian ice age [110]. As ice sheets continued to form, the climate became colder and drier [101].

Stage 4 corresponds to biozones LM1 and LM4, in which the banded silty sand horizontal bedding contains siliceous shale. During this period, the quartz content reached its peak (averaging 53.76%), whereas the carbonate mineral content reached its lowest point (averaging 13.41%). The clay mineral content was notably reduced, decreasing to an average of 25.75%. These observations indicate the presence of abundant OM, with minimal terrestrial input. This provided good conditions for the extensive accumulation and preservation of OM. Earlier, the melting of the Gondwanan continental glaciers caused a rapid rise in sea level, resulting in widespread transgression [7,111–114]. These conclusions were supported by the CIA values (increases from 66.38 to 73.31). During this period, marine plankton flourished, and the low terrestrial input was conducive to the formation of the organic-rich black shale with a thickness of tens of meters [19]. The change in the SiO_2 content was incompatible with TiO_2 and Al_2O_3 , also illustrating that SiO_2 was mainly derived from biogenic silica [115]. As TOC increased from 0.92% to 4.52%, the corresponding terrestrial input parameters showed a clear downward trend over the same period. In the later phase of Block 4, increases in TiO_2 , Al_2O_3 , and ΣREE were accompanied by small fluctuations, showing an increasing quantity of terrestrial influx. The decrease in TOC content indicates that the enrichment of OM is weakened. As the Caledonian movement of the Cathaysian Plate continued to advance northwest, the Qianzhong–Xuefeng zone was uplifted and eroded, increasing the supply of nutrients transported to the ocean from clastic sediments and inhibiting the deposition of organic-rich shale [19,20,30,101].

Stage 5 corresponds to biozone LM5 (silty shale). During this stage, the quartz content began to decrease (averaging 36.77%), whereas the carbonate mineral and clay mineral contents increased gradually (averaging 16.76% and 32.9%, respectively). Overall, terrestrial input remained high. Additionally, there was a noticeable decrease in the TOC content, ranging from 1.16% to 2.16%, with an average of 1.73%. In the Early Silurian strata of the upper Yangtze region, the possible small glacial events of the Early Aeronian were related to large Rhuddanian organic carbon sequestration, leading to the removal of a large quantity of ^{12}C in the marine system [116–118]. The overall abrupt changes in CIA, ICV, Cs/Ti, and Rb/Ti in Block 5 indicate a low chemical weathering intensity and cold and dry climate conditions. The sea level fluctuations in the Upper Yangtze Block are not fully in accordance with global sea level variations, which may be related to strong tectonic activity that has altered the basin-mountain pattern of the South China Plate [19,119]. During this period, OM enrichment was limited because of stable and continuously high terrestrial input.

Stage 6 corresponds to biozones LM6–8, characterized by interbedded silty and clay lamina. During this interval, the quartz content remained at a low level, averaging 41.4%. The contents of carbonate minerals and clay minerals continued to increase, with average values of 10.26% and 40.45%, respectively. The TOC remained low (0.83%–2.27%; average, 1.53%). However, despite the maximum average CIA index reaching 69%, the increase in temperature did not lead to a proportionate increase in organic matter abundance. In summary, the influence of terrigenous influx was significantly greater than that of environmental change. During the study period, the continuous uplift of Leshan–Longnvsi and Qianzhong–Xuefeng contributed to the effective supply of terrigenous materials. The enrichment of OM weakened under the conditions of a large supply of terrigenous clastic materials. Therefore, the injection of terrigenous debris has a significant destructive effect on OM enrichment.

6. Conclusions

Based on analyses of TOC content and sedimentary geochemical indicators of organic-rich shales in the Wufeng–Longmaxi Formation in the southern Sichuan Basin, the following conclusions have been drawn.

- (1) The Wufeng–Longmaxi shale in the study area is mainly composed of quartz, calcite, dolomite, and clay minerals. The graptolite zones LM1–4 are predominantly siliceous shale, with high TOC contents. Corresponding to the banded silty sand horizontal bedding are amorphous organic matter, high bio-quartz contents, and low terrigenous clay mineral and carbonate mineral contents.
- (2) The Wufeng–Longmaxi shale is the first cyclic deposit and presents immature mineral compositions. The original geochemical properties exhibit sedimentary sorting and limited changes, rendering the shale an effective indicator for provenance and for tectonic setting analyses.
- (3) Source rocks, as sediments, are initially deposited during tectonic activity. The paleoweathering intensity and paleoclimate characteristics from the Wufeng Formation to the lower section of the Longmaxi Formation underwent two abrupt changes, exhibiting gradually increasing weathering under warm and humid climates of moderate intensity overall. During diagenesis, potassium metamorphism exerted minimal impact on the rocks.
- (4) The provenance of Wufeng–Longmaxi shale can be traced back to igneous rocks originated from the active continental margin, especially from continental collision (extrusion).
- (5) Based on a comprehensive analysis of paleoclimate and paleoprovenance characteristics, we identified six stages of evolution in the Wufeng–Longmaxi Formation. The stage of relative enrichment of organic matter corresponds to LM1, LM2–3, and LM4. The period coincided with the post-Hirnantian glacial period of global warming, glacier melting, a rise in global sea level, and a decrease in terrestrial debris supply, which likely facilitated organic matter enrichment. However, during the LM5 and

LM6–8 stages, the continuous uplift of the Leshan–Longnsvi and Qianzhong–Xuefeng area contributed to the effective supply of materials, thereby suppressing organic matter enrichment.

Supplementary Materials: The following supporting information can be downloaded at: <https://www.mdpi.com/article/10.3390/min13121502/s1>, Table S1: Mineral compositions and TOC content of the Wufeng–Longmaxi shale in the southern Sichuan Basin, China; Table S2: Concentrations of major element oxides of the Wufeng–Longmaxi shale in the southern Sichuan Basin, China; Table S3: Concentrations of trace elements (in ppm) in the Wufeng–Longmaxi shale in the southern Sichuan Basin, China.

Author Contributions: Conceptualization, L.Q., H.W. and Z.S.; data curation, L.Q. and F.C.; formal analysis, L.Q.; validation, L.Q., T.Z. and G.L.; writing—original draft preparation, L.Q.; writing—review and editing, L.Q.; resources, H.W. and Z.S.; funding acquisition, H.W. and Z.S.; software, T.Z.; project administration, S.S. All authors have read and agreed to the published version of the manuscript.

Funding: This research was funded by the 14th Five-Year Plan of the Ministry of Science and Technology of PetroChina, grant number: 2021DJ1901.

Data Availability Statement: The data that support the findings of this study are available from the corresponding author upon reasonable request.

Conflicts of Interest: The authors declare no conflict of interest.

References

- Zou, C.; Zhao, Q.; Cong, L.; Wang, H.; Shi, Z.; Wu, J.; Pan, S. Development progress, potential and prospect of shale gas in China. *Nat. Gas Ind.* **2021**, *41*, 1–14. [[CrossRef](#)]
- Ma, X.; Zhang, X.; Xiong, W.; Liu, Y.; Gao, J.; Yu, R.; Sun, Y.; Wu, J.; Kang, L.; Zhao, S. Prospects and challenges of shale gas development in China. *Petrol. Sci. Bull.* **2023**, *04*, 491–501.
- He, X.; Chen, G.; Wu, J.; Liu, Y.; Wu, S.; Zhang, J.; Zhang, X. Deep shale gas exploration and development in the southern Sichuan Basin: New progress and challenges. *Nat. Gas Ind.* **2023**, *10*, 32–43. [[CrossRef](#)]
- Lüning, S.; Craig, J.; Loydell, D.K.; Štorch, P.; Fitches, B. Lower Silurian ‘hot shales’ in North Africa and Arabia: Regional distribution and depositional model. *Earth Sci. Rev.* **2000**, *49*, 121–200. [[CrossRef](#)]
- Wu, Y.; Fan, T.; Jiang, S.; Yang, X.; Ding, H.; Meng, M.; Wei, D. Methane adsorption capacities of the Lower Paleozoic marine shales in the Yangtze platform, South China. *Energy Fuels* **2015**, *29*, 4160–4167. [[CrossRef](#)]
- Ge, X.; Mou, C.; Yu, Q.; Liu, W.; Men, X.; He, J. The geochemistry of the sedimentary rocks from the Huadi No. 1 well in the Wufeng-Longmaxi formations (Upper Ordovician-Lower Silurian), South China, with implications for paleoweathering, provenance, tectonic setting and paleoclimate. *Mar. Petrol. Geol.* **2019**, *103*, 646–660. [[CrossRef](#)]
- Zhou, L.; Algeo, T.J.; Shen, J.; Hu, Z.; Gong, H.; Xie, S.; Huang, J.; Gao, S. Changes in marine productivity and redox conditions during the Late Ordovician Hirnantian glaciation. *Palaeogeogr. Palaeoclimatol. Palaeoecol.* **2015**, *420*, 223–234. [[CrossRef](#)]
- Wu, H. Reinterpretation of the Guangxian orogeny. *Chin. Sci. Bull.* **2000**, *45*, 1244–1248. [[CrossRef](#)]
- Munnecke, A.; Calner, M.; Harper, D.A.; Servais, T. Ordovician and Silurian sea-water chemistry, sea level, and climate: A synopsis. *Palaeogeogr. Palaeoclimatol. Palaeoecol.* **2010**, *296*, 389–413. [[CrossRef](#)]
- Lu, L.; Qin, J.; Shen, B.; Tenger, Liu, W.; Zhang, Q. The origin of biogenic silica in siliceous shale from Wufeng-Longmaxi Formation in the Middle and Upper Yangtze region and its relationship with shale gas enrichment. *Earth Sci. Front.* **2018**, *25*, 226–236. [[CrossRef](#)]
- Zhao, J.; Jin, Z.; Jin, Z.; Wen, X.; Geng, Y.; Yan, C. The genesis of quartz in Wufeng-Longmaxi gas shales, Sichuan Basin. *Nat. Gas Geosci.* **2016**, *27*, 377–386.
- Zhou, X.F.; Li, X.Z.; Guo, W.; Zhang, X.; Liang, P.; Yu, J. Characteristics, formation mechanism and influence on physical properties of carbonate minerals in shale reservoir of Wufeng-Longmaxi formations, Sichuan Basin. *J. Nat. Gas Geosci.* **2022**, *33*, 775–788. [[CrossRef](#)]
- Chen, L.; Lu, Y.; Jiang, S.; Li, J.; Guo, T.; Luo, C. Heterogeneity of the Lower Silurian Longmaxi marine shale in the southeast Sichuan Basin of China. *Mar. Petrol. Geol.* **2015**, *65*, 232–246. [[CrossRef](#)]
- Han, S.; Zhang, J.; Wang, C.; Tang, X. Elemental geochemistry of Lower Silurian Longmaxi shale in southeast Sichuan Basin, South China: Constraints for Paleoenvironment. *Geol. J.* **2018**, *53*, 1458–1464. [[CrossRef](#)]
- Baioumy, H.; Ulfa, Y.; Nawawi, M.; Padmanabhan, E.; Anuar, M.N.A. Mineralogy and geochemistry of Palaeozoic black shales from Peninsular Malaysia: Implications for their origin and maturation. *Int. J. Coal Geol.* **2016**, *165*, 90–105. [[CrossRef](#)]
- Negri, A.; Ferretti, A.; Wagner, T.; Meyers, P.A. Phanerozoic organic-carbon-rich marine sediments: Overview and future research challenges. *Palaeogeogr. Palaeoclimatol. Palaeoecol.* **2009**, *273*, 218–227. [[CrossRef](#)]

17. Yan, D.; Chen, D.; Wang, Q.; Wang, J. Large-scale climatic fluctuations in the latest Ordovician on the Yangtze block, south China. *Geology* **2010**, *38*, 599–602. [[CrossRef](#)]
18. Zhao, J.; Jin, Z.; Jin, Z.; Geng, Y.; Wen, X.; Yan, C. Applying sedimentary geochemical proxies for paleoenvironment interpretation of organic-rich shale deposition in the Sichuan Basin, China. *Int. J. Coal Geol.* **2016**, *163*, 52–71. [[CrossRef](#)]
19. Huang, H.; He, D.; Li, D.; Li, Y.; Zhang, W.; Chen, J. Geochemical characteristics of organic-rich shale, Upper Yangtze Basin: Implications for the Late Ordovician-Early Silurian orogeny in South China. *Palaeogeogr. Palaeoclimatol. Palaeoecol.* **2020**, *554*, 109822. [[CrossRef](#)]
20. Ding, M.; Li, Y.; Fan, T.; Lash, G.; Wei, X.; Zhang, T. Geochemistry of the Lower Silurian black shales from the Upper Yangtze Platform, South China: Implications for paleoclimate, provenance, and tectonic setting. *J. Asian Earth Sci.* **2023**, *242*, 105493. [[CrossRef](#)]
21. Men, X.; Mou, C.; Ge, X. Changes in palaeoclimate and palaeoenvironment in the Upper Yangtze area (South China) during the Ordovician-Silurian transition. *Sci. Rep.* **2022**, *12*, 13186. [[CrossRef](#)]
22. Basu, A.; Bickford, M.E.; Deasy, R. Inferring tectonic provenance of siliciclastic rocks from their chemical compositions: A dissent. *Sediment. Geol.* **2016**, *336*, 26–35. [[CrossRef](#)]
23. Cullers, R.L.; Chaudhuri, S.; Arnold, B.; Lee, M.; Wolf, C.W. Rare earth distributions in clay minerals and in the clay-sized fraction of the Lower Permian Havensville and Eskridge shales of Kansas and Oklahoma. *Geochim. Cosmochim. Acta* **1975**, *39*, 1691–1703. [[CrossRef](#)]
24. Taylor, S.R.; McLennan, S.M. *The Continental Crust: Its Composition and Evolution*; Blackwell Scientific Publications: Palo Alto, CA, USA, 1985.
25. Bhatia, M.R.; Crook, K.A.W. Trace element characteristics of graywackes and tectonic setting discrimination of sedimentary basins. *Contrib. Mineral. Petrol.* **1986**, *92*, 181–193. [[CrossRef](#)]
26. Hayashi, K.I.; Fujisawa, H.; Holland, H.D.; Ohmoto, H. Geochemistry of approximately 1.9 ga sedimentary rocks from northeastern Labrador, Canada. *Geochim. Cosmochim. Acta* **1997**, *61*, 4115–4137. [[CrossRef](#)] [[PubMed](#)]
27. Chen, W.; Tian, J.; Lin, X.; Liang, Q.; Wang, X.; Yi, D.; Li, Y. Climate fluctuations during the Ordovician-Silurian transition period in South China: Implications for paleoenvironmental evolution and organic matter enrichment. *Palaeogeogr. Palaeoclimatol. Palaeoecol.* **2023**, *613*, 111411. [[CrossRef](#)]
28. Wang, Y.; Ge, X.; Mou, C.; Liang, W.; Men, X. Sedimentary and geochemical responses to the end Ordovician glaciation in the Guanyinqiao formation (Late Ordovician-Early Silurian period) in the Sichuan Basin. *Geochem. Int.* **2022**, *60*, 641–656. [[CrossRef](#)]
29. Yan, D.; Li, S.; Fu, H.; Jasper, D.M.; Zhou, S.; Yang, X.; Zhang, B.; Mangi, H.N. Mineralogy and geochemistry of Lower Silurian black shales from the Yangtze platform, South China. *Int. J. Coal Geol.* **2021**, *237*, 103706. [[CrossRef](#)]
30. Zan, B.; Mou, C.; Lash, G.G.; Ge, X.; Wang, X.; Wang, Q.; Yan, J.; Chen, F.; Jin, B. An integrated study of the petrographic and geochemical characteristics of organic-rich deposits of the Wufeng and Longmaxi formations, western Hubei Province, South China: Insights into the co-evolution of paleoenvironment and organic matter accumulation. *Mar. Petrol. Geol.* **2021**, *132*, 105193. [[CrossRef](#)]
31. Yu, J.; O'Reilly, S.Y.; Wang, L.; Griffin, W.L.; Zhang, M.; Wang, R.; Jiang, S.; Shu, L. Where was South China in the Rodinia supercontinent? *Precambrian Res.* **2008**, *164*, 1–15. [[CrossRef](#)]
32. Zhou, L.; Kang, Z.; Wang, Z.; Peng, Y.; Xiao, H. Sedimentary geochemical investigation for paleoenvironment of the Lower Cambrian Niutitang Formation shales in the Yangtze Platform. *J. Petrol. Sci. Eng.* **2017**, *159*, 376–386. [[CrossRef](#)]
33. Guo, Y.H.; Li, Z.F.; Li, D.H.; Zhang, T.M.; Wang, Z.C.; Yu, J.F.; Xi, Y.T. Lithofacies palaeogeography of the Early Silurian in Sichuan area. *J. Palaeogeogr.* **2004**, *6*, 20–29. [[CrossRef](#)]
34. Shi, Z.; Wang, H.; Sun, S.; Guo, C. Graptolite zone calibrated stratigraphy and topography of the Late Ordovician-Early Silurian Wufeng-Lungmachi shale in Upper Yangtze area, South China. *Arab. J. Geosci.* **2021**, *14*, 213. [[CrossRef](#)]
35. Shi, Z.; Zhou, T.; Wang, H.; Sun, S. Depositional structures and their reservoir characteristics in the Wufeng-Longmaxi shale in Southern Sichuan Basin, China. *Energies* **2022**, *15*, 1618. [[CrossRef](#)]
36. Wang, H.; Shi, Z.; Sun, S. Biostratigraphy and reservoir characteristics of the Ordovician Wufeng Formation—Silurian Longmaxi Formation shale in the Sichuan Basin and its surrounding areas, China. *Petrol. Explor. Dev.* **2021**, *48*, 1019–1032. [[CrossRef](#)]
37. Gromet, L.P.; Haskin, L.A.; Korotev, R.L.; Dymek, R.F. The “North American shale composite”: Its compilation, major and trace element characteristics. *Geochim. Cosmochim. Acta* **1984**, *48*, 2469–2482. [[CrossRef](#)]
38. Nesbitt, H.W.; Young, G.M. Early Proterozoic climates and plate motions inferred from major element chemistry of lutites. *Nature* **1982**, *299*, 715–717. [[CrossRef](#)]
39. McLennan, S.M.; Hemming, S.; McDaniell, D.K.; Hanson, G.N. Geochemical approaches to sedimentation, provenance, and tectonics. In *Processes Controlling the Composition of Clastic Sediments*; Johnsson, M.J., Basu, A., Eds.; Geological Society of America: Boulder, CO, USA, 1993; Volume 284, pp. 21–40. [[CrossRef](#)]
40. Nesbitt, H.W.; Young, G.M. Prediction of some weathering trends of plutonic and volcanic rocks based on thermodynamic and kinetic considerations. *Geochim. Cosmochim. Acta* **1984**, *48*, 1523–1534. [[CrossRef](#)]
41. Young, G.M.; Wayne Nesbitt, H. Paleoclimatology and provenance of the glaciogenic Gowganda Formation (Paleoproterozoic), Ontario, Canada: A chemostratigraphic approach. *GSA Bull.* **1999**, *111*, 264–274. [[CrossRef](#)]
42. Cullers, R.L.; Podkovyrov, V.N. Geochemistry of the Mesoproterozoic Lakhanda shales in southeastern Yakutia, Russia: Implications for mineralogical and provenance control, and recycling. *Precambrian Res.* **2000**, *104*, 77–93. [[CrossRef](#)]

43. Cullers, R.L.; Podkovyrov, V.N. The source and origin of terrigenous sedimentary rocks in the Mesoproterozoic Ui group, southeastern Russia. *Precambrian Res.* **2002**, *117*, 157–183. [[CrossRef](#)]
44. Wang, H.; Dong, D.; Shi, Z. Lithfacies and “sweet spot” interval of marine shale in southern Sichuan: A case study of Shuanghe Outcrop in Wufeng-Longmaxi Formation, Changning. *Petrol. Reservoir Eval. Dev.* **2022**, *12*, 68–81. [[CrossRef](#)]
45. Tang, L.; Song, Y.; Zhao, Z. Origin and evolution of overpressure in shale gas reservoirs of the Upper Ordovician Wufeng Formation-Lower Silurian Longmaxi Formation in the Sichuan Basin. *Nat. Gas Ind.* **2022**, *42*, 37–53.
46. Meng, J.; Lyu, P.; Wu, W. A method for evaluating the thermal maturity of marine shale based on graptolite reflectance and Raman spectroscopy: A case from the Lower Palaeozoic Wufeng-Longmaxi Formations, southern Sichuan Basin, SW China. *Oil Gas Geol.* **2022**, *43*, 1515–1528. [[CrossRef](#)]
47. Shi, Z.S.; Qiu, Z.; Dong, D.Z.; Lu, B.; Liang, P.P.; Zhang, M.Q. Lamina characteristics of gas-bearing shale fine-grained sediment of the Silurian Longmaxi Formation of Well Wuxi 2 in Sichuan Basin, SW China. *Petrol. Explor. Dev.* **2018**, *45*, 358–368. [[CrossRef](#)]
48. Liu, G.; Zhai, G.; Yang, R.; He, T.; Wei, B. Quartz crystallinity index: New quantitative evidence for biogenic silica of the Late Ordovician to Early Silurian organic-rich shale in the Sichuan Basin and adjacent areas, China. *Sci. China Earth Sci.* **2021**, *64*, 773–787. [[CrossRef](#)]
49. Shi, Z.; Zhou, T.; Guo, W.; Liang, P.; Cheng, F. Quantitative paleogeographic mapping and sedimentary microfacies division in a deep-water marine shale shelf: Case study of Wufeng Formation-Longmaxi formation shale, southern sichuan basin, China. *Acta Sedimentol. Sin.* **2022**, *40*, 1729–1744.
50. Hower, J.; Eslinger, E.; Hower, M.; Perry, E. Mechanism of burial metamorphism of argillaceous sediment—Mineralogical and chemical evidence. *Geol. Soc. Am. Bulletin.* **1976**, *87*, 725–737. [[CrossRef](#)]
51. Wang, Y.; Li, X.; Chen, B.; Wu, W.; Dong, D.; Zhang, J. Lower limit of thermal maturity for the carbonization of organic matter in marine shale and its exploration risk. *Petrol. Explor. Dev.* **2018**, *45*, 385–395. [[CrossRef](#)]
52. Zhang, G.; Nie, H.; Tang, X.; Du, W. Pyrite type and its effect on shale gas accumulation: A case study of Wufeng-Longmaxi shale in Sichuan Basin and its periphery. *Petrol. Geol. Exp.* **2020**, *42*, 459–466.
53. Chen, Q. Study on authigenic pyrites in sediments of the South Huanghai Sea. *Acta Geol. Sin.* **1981**, *3*, 232–246. [[CrossRef](#)]
54. Chang, H.; Chu, X.L.; Feng, L.; Huang, J. Framboidal pyrites in cherts of the laobao formation, south china: Evidence for anoxic deep ocean in the terminal ediacaran. *Acta Petrol. Sin.* **2009**, *25*, 1001–1007. [[CrossRef](#)]
55. Chang, X.; Zhang, M.; Gu, Y.; Wang, H.; Liu, X. Formation mechanism and controlling factors of authigenic pyrite in mud sediments on the shelf of the Yellow Sea and the East China Sea. *Adv. Earth Sci.* **2020**, *35*, 1306–1320. [[CrossRef](#)]
56. Bond, D.P.G.; Wignall, P.B. Pyrite framboid study of marine Permian–Triassic boundary sections: A complex anoxic event and its relationship to contemporaneous mass extinction. *GSA Bulletin.* **2010**, *122*, 1265–1279. [[CrossRef](#)]
57. Chen, X.; Chen, L.; Tan, X.; Jiang, S.; Wang, C. Impact of pyrite on shale gas enrichment—A case study of the Lower Silurian Longmaxi Formation in southeast Sichuan Basin. *Front. Earth Sci.* **2021**, *15*, 332–342. [[CrossRef](#)]
58. Yang, X.; Gong, Y. Pyrite Framboid: Indicator of Environments and Life. *Earth Sci.* **2011**, *36*, 643–658.
59. Canfield, D.; Thamdrup, B. The production of 34S-depleted sulfide during bacterial disproportionation of elemental sulfur. *Science* **1994**, *266*, 1973–1975. [[CrossRef](#)]
60. Fisher, I.; Hudson, J. Pyrite formation in Jurassic shales of contrasting biofacies. *Geol. Soc. Lond. Spec. Publ.* **1987**, *26*, 69–78. [[CrossRef](#)]
61. Jiang, K.; Zhou, W.; Deng, N.; Zhang, H.T.; Xu, H.; Zhao, X.; Yi, T.; Yang, F. Characteristics and geological significance of pyrites in Wufeng and Longmaxi Formation reservoir shale in Sichuan Basin, China. *J. Chengfu Univ. Technol.* **2020**, *47*, 50–64. [[CrossRef](#)]
62. Li, Q.G.; Liu, S.W.; Wang, Z.Q.; Chu, Z.Y.; Song, B.; Wang, Y.B.; Wang, T. Contrasting provenance of Late Archean metasedimentary rocks from the Wutai Complex, North China Craton: Detrital zircon U-Pb, whole-rock Sm-Nd isotopic, and geochemical data. *Int. J. Earth Sci.* **2008**, *97*, 443–458. [[CrossRef](#)]
63. Cullers, R.L. Mineralogical and chemical changes of soil and stream sediment formed by intense weathering of the Danburg granite, Georgia, U.S.A. *Lithos* **1988**, *21*, 301–314. [[CrossRef](#)]
64. McLennan, S.M.; Taylor, S.R.; McCulloch, M.T.; Maynard, J.B. Geochemical and Nd-Sr isotopic composition of deep-sea turbidites: Crustal evolution and plate tectonic associations. *Geochim. Cosmochim. Acta* **1990**, *54*, 2015–2050. [[CrossRef](#)]
65. Garcia, D.; Fonteilles, M.; Moutte, J. Sedimentary fractionations between Al, Ti, and Zr and the genesis of strongly peraluminous granites. *J. Geol.* **1994**, *102*, 411–422. [[CrossRef](#)]
66. La Flèche, M.R.; Camiré, G. Geochemistry and provenance of metasedimentary rocks from the Archean Golden Pond sequence (Casa Berardi mining district, Abitibi subprovince). *Can. J. Earth Sci.* **1996**, *33*, 676–690. [[CrossRef](#)]
67. Li, Q.; Liu, S.; Han, B.; Zhang, J.; Chu, Z. Geochemistry of metasedimentary rocks of the Proterozoic Xingxingxia complex: Implications for provenance and tectonic setting of the eastern segment of the Central Tianshan Tectonic Zone, northwestern China. *Can. J. Earth Sci.* **2005**, *42*, 287–306. [[CrossRef](#)]
68. McLennan, S.M. Rare earth elements in sedimentary rocks: Influence of provenance and sedimentary processes. *Rev. Mineral. Geochem.* **1989**, *21*, 169–200.
69. Cullers, R.L. The chemical signature of source rocks in size fractions of Holocene stream sediment derived from metamorphic rocks in the Wet Mountains region, Colorado, U.S.A. *Chem. Geol.* **1994**, *113*, 327–343. [[CrossRef](#)]
70. Fadipe, O.A.; Carey, P.F.; Akinlua, A.; Adekola, S.A. Provenance, diagenesis and reservoir quality of the Lower Cretaceous sandstone of the Orange Basin, South Africa. *S. Afr. J. Geol.* **2011**, *114*, 433–448. [[CrossRef](#)]

71. Panahi, A.; Young, G.M.; Rainbird, R.H. Behavior of major and trace elements (including REE) during Paleoproterozoic pedogenesis and diagenetic alteration of an Archean granite near Ville Marie, Quebec, Canada. *Geochim. Cosmochim. Acta* **2000**, *64*, 2199–2220. [[CrossRef](#)]
72. Nesbitt, H.W.; Young, G.M.; McLennan, S.M.; Keays, R.R. Effects of chemical weathering and sorting on the petrogenesis of siliciclastic sediments, with implications for provenance studies. *J. Geol.* **1996**, *104*, 525–542. [[CrossRef](#)]
73. Aldega, L.; Brandano, M.; Cornaccina, I. Trophism, climate and paleoweathering conditions across the Eocene-Oligocene transition in the Massignano section (northern Apennines, Italy). *Sediment. Geol.* **2020**, *405*, 105701. [[CrossRef](#)]
74. Deepthi, K.; Natesan, U.; Muthulakshmi, A.L.; Ferrer, V.A.; Venugopalan, V.P.; Narasimhan, S.V. Geochemical characteristics and depositional environment of Kalpakkam, southeast coast of India. *Environ. Earth Sci.* **2013**, *69*, 2357–2364. [[CrossRef](#)]
75. Ghosh, S.; Sarkar, S.; Ghosh, P. Petrography and major element geochemistry of the Permo-Triassic sandstones, central India: Implications for provenance in an intracratonic pull-apart basin. *J. Asian Earth Sci.* **2012**, *43*, 207–240. [[CrossRef](#)]
76. Fedo, C.M.; Eriksson, K.A.; Krogstad, E.J. Geochemistry of shales from the Archean (~3.0 ga) Buhwa Greenstone Belt, Zimbabwe: Implications for provenance and source-area weathering. *Geochim. Cosmochim. Acta* **1996**, *60*, 1751–1763. [[CrossRef](#)]
77. Chaudhuri, S.; Cullers, R.L. The distribution of rare-earth elements in deeply buried Gulf Coast sediments. *Chem. Geol.* **1979**, *24*, 327–338. [[CrossRef](#)]
78. Gao, S.; Wedepohl, K.H. The negative Eu anomaly in Archean sedimentary rocks: Implications for decomposition, age and importance of their granitic sources. *Earth Planet. Sci. Lett.* **1995**, *133*, 81–94. [[CrossRef](#)]
79. Cullers, R.L.; Bock, B.; Guidotti, C. Elemental distributions and neodymium isotopic compositions of Silurian metasediments, western Maine, USA: Redistribution of the rare earth elements. *Geochim. Cosmochim. Acta* **1997**, *61*, 1847–1861. [[CrossRef](#)]
80. Floyd, P.A.; Leveridge, B.E. Tectonic environment of the Devonian Gramscatho basin, south Cornwall: Framework mode and geochemical evidence from turbiditic sandstones. *J. Geol. Soc.* **1987**, *144*, 531–542. [[CrossRef](#)]
81. Armstrong-Altrin, J.S.; Verma, S.P. Critical evaluation of six tectonic setting discrimination diagrams using geochemical data of Neogene sediments from known tectonic settings. *Sediment. Geol.* **2005**, *177*, 115–129. [[CrossRef](#)]
82. Purevjav, N.; Roser, B. Geochemistry of Devonian-Carboniferous clastic sediments of the Tsetserleg terrane, Hangay Basin, Central Mongolia: Provenance, source weathering, and tectonic setting. *Isl. Arc* **2012**, *21*, 270–287. [[CrossRef](#)]
83. Roser, B.P.; Korsch, R.J. Determination of tectonic setting of sandstone-mudstone suites using SiO₂ content and K₂O/Na₂O ratio. *J. Geol.* **1986**, *94*, 635–650. [[CrossRef](#)]
84. Tao, H.; Sun, S.; Wang, Q.; Yang, X.; Jiang, L. Petrography and geochemistry of lower carboniferous greywacke and mudstones in Northeast Junggar, China: Implications for provenance, source weathering, and tectonic setting. *J. Asian Earth Sci.* **2014**, *87*, 11–25. [[CrossRef](#)]
85. Verma, S.P.; Armstrong-Altrin, J.S. New multi-dimensional diagrams for tectonic discrimination of siliciclastic sediments and their application to Precambrian basins. *Chem. Geol.* **2013**, *355*, 117–133. [[CrossRef](#)]
86. Verma, S.P.; Armstrong-Altrin, J.S. Geochemical discrimination of siliciclastic sediments from active and passive margin settings. *Sediment. Geol.* **2016**, *332*, 1–12. [[CrossRef](#)]
87. Zaid, S.M. Geochemistry of sandstones from the Pliocene Gabir Formation, north Marsa Alam, Red Sea, Egypt: Implication for provenance, weathering and tectonic setting. *J. Afr. Earth Sci.* **2015**, *102*, 1–17. [[CrossRef](#)]
88. Bhatia, M.R. Plate tectonics and geochemical composition of sandstones. *J. Geol.* **1983**, *91*, 611–627. [[CrossRef](#)]
89. Canfield, D.E. Factors influencing organic carbon preservation in marine sediments. *Chem. Geol.* **1994**, *114*, 315–329. [[CrossRef](#)]
90. Ibach, L.E.J. Relationship between sedimentation rate and total organic carbon content in ancient marine sediments. *Am. Assoc. Petrol. Geol. Bull.* **1982**, *66*, 170–188. [[CrossRef](#)]
91. Rimmer, S.M. Geochemical paleoredox indicators in Devonian-Mississippian black shales, Central Appalachian Basin (USA). *Chem. Geol.* **2004**, *206*, 373–391. [[CrossRef](#)]
92. Calvert, S.E.; Pedersen, T.F. Geochemistry of recent oxic and anoxic marine sediments: Implications for the geological record. *Mar. Geol.* **1993**, *113*, 67–88. [[CrossRef](#)]
93. Kidder, D.L.; Erwin, D.H. Secular distribution of biogenic silica through the Phanerozoic: Comparison of silica-replaced fossils and bedded cherts at the series level. *J. Geol.* **2001**, *109*, 509–522. [[CrossRef](#)]
94. Murray, R.W.; Leinen, M. Chemical transport to the seafloor of the equatorial Pacific Ocean across a latitudinal transect at 135°W: Tracking sedimentary major, trace, and rare earth element fluxes at the Equator and the Intertropical Convergence Zone. *Geochim. Cosmochim. Acta* **1993**, *57*, 4141–4163. [[CrossRef](#)]
95. Wang, C.; Wang, Q.; Chen, G.; He, L.; Xu, Y.; Chen, L.; Chen, D. Petrographic and geochemical characteristics of the lacustrine black shales from the Upper Triassic Yanchang Formation of the Ordos Basin, China: Implications for the organic matter accumulation. *Mar. Petrol. Geol.* **2017**, *86*, 52–65. [[CrossRef](#)]
96. Yan, D.; Wang, H.; Fu, Q.; Chen, Z.; He, J.; Gao, Z. Geochemical characteristics in the Longmaxi Formation (Early Silurian) of South China: Implications for organic matter accumulation. *Mar. Petrol. Geol.* **2015**, *65*, 290–301. [[CrossRef](#)]
97. Lu, Y.; Jiang, S.; Lu, Y.; Xu, S.; Shu, Y.; Wang, Y. Productivity or preservation? The factors controlling the organic matter accumulation in the Late Katian through Hirnantian Wufeng organic-rich shale, South China. *Mar. Petrol. Geol.* **2019**, *109*, 22–35. [[CrossRef](#)]

98. Shi, Z.; Zhao, S.; Zhou, T.; Ding, L.; Sun, S.; Cheng, F. Mineralogy and geochemistry of the Upper Ordovician and Lower Silurian Wufeng–Longmaxi shale on the Yangtze platform, South China: Implications for provenance analysis and shale gas sweet-spot interval. *Minerals* **2022**, *12*, 1190. [[CrossRef](#)]
99. Nesbitt, H.; Markovics, G. Chemical processes affecting alkalis and alkaline earths during continental weathering. *Geochim. Et Cosmochim. Acta* **1980**, *44*, 1659–1666. [[CrossRef](#)]
100. Yan, Y.; Xia, B.; Lin, G.; Cui, X. Geochemistry of the sedimentary rocks from the Nanxiong Basin, South China and implications for provenance, paleoenvironment and paleoclimate at the K/T boundary. *Sediment. Geol.* **2007**, *197*, 127–140. [[CrossRef](#)]
101. Wang, X.; Zhu, Y.; Lash, G.G.; Wang, Y. Multi-proxy analysis of organic matter accumulation in the Upper Ordovician-Lower Silurian black shale on the Upper Yangtze Platform, south China. *Mar. Petrol. Geol.* **2019**, *103*, 473–484. [[CrossRef](#)]
102. Xu, C.; Jia-Yu, R.; Yue, L.; Boucot, A.J. Facies patterns and geography of the Yangtze region, South China, through the Ordovician and Silurian transition. *Palaeogeogr. Palaeoclimatol. Palaeoecol.* **2004**, *204*, 353–372. [[CrossRef](#)]
103. Armstrong, H.A.; Turner, B.R.; Makhlof, I.M.; Weedon, G.P.; Williams, M.; Al Smadi, A.; Abu Salah, A. Origin, sequence stratigraphy and depositional environment of an Upper Ordovician (Hirnantian) deglacial black shale, Jordan. *Palaeogeogr. Palaeoclimatol. Palaeoecol.* **2005**, *220*, 273–289. [[CrossRef](#)]
104. Delabroye, A.; Vecoli, M. The end-Ordovician glaciation and the Hirnantian Stage: A global review and questions about Late Ordovician event stratigraphy. *Earth Sci. Rev.* **2010**, *98*, 269–282. [[CrossRef](#)]
105. Haq, B.U.; Schutter, S.R. A chronology of Paleozoic sea-level changes. *Science* **2008**, *322*, 64–68. [[CrossRef](#)]
106. Le Heron, D.P.; Ghienne, J.; El Houicha, M.; Khoukhi, Y.; Rubino, J. Maximum extent of ice sheets in Morocco during the Late Ordovician glaciation. *Palaeogeogr. Palaeoclimatol. Palaeoecol.* **2007**, *245*, 200–226. [[CrossRef](#)]
107. Lu, Y.; Huang, C.; Jiang, S.; Zhang, J.; Lu, Y.; Liu, Y. Cyclic Late Katian through Hirnantian glacioeustasy and its control of the development of the organic-rich Wufeng and Longmaxi shales, South China. *Palaeogeogr. Palaeoclimatol. Palaeoecol.* **2019**, *526*, 96–109. [[CrossRef](#)]
108. Pohl, A.; Austermann, J. A sea-level fingerprint of the Late Ordovician ice-sheet collapse. *Geology* **2018**, *46*, 595–598. [[CrossRef](#)]
109. Chen, X.; Rong, J.Y.; Fan, J.X.; Zhan, R.B.; Mitchell, C.E.; Harper, D.A.T.; Melchin, M.J.; Peng, P.A.; Finney, S.C.; Wang, X.F. A final report on the global stratotype section and point (GSSP) for the Hirnantian Stage (Upper Ordovician). *J. Stratigr.* **2006**, *30*, 289–307.
110. Wang, Y.; Dong, D.; Huang, J.; Li, X.; Wang, S.; Guan, Y.Q. Member lithofacies of the Upper Ordovician Wufeng Formation around the Sichuan Basin and the significance to shale gas plays, SW China. *Petrol. Explor. Dev.* **2016**, *43*, 42–50. [[CrossRef](#)]
111. Brenchley, P.J.; Marshall, J.D.; Carden, G.A.F.; Robertson, D.B.R.; Long, D.G.F.; Meidla, T.; Hints, L.; Anderson, T.F. Bathymetric and isotopic evidence for a short-lived Late Ordovician glaciation in a greenhouse period. *Geology* **1994**, *22*, 295–298. [[CrossRef](#)]
112. Fan, J.; Peng, P.; Melchin, M.J. Carbon isotopes and event stratigraphy near the Ordovician-Silurian boundary, Yichang, South China. *Palaeogeogr. Palaeoclimatol. Palaeoecol.* **2009**, *276*, 160–169. [[CrossRef](#)]
113. Meng, C.; Hu, W.; Jia, D.; Wang, L. Analyses of geochemistry features and sedimentary environment in the Upper Ordovician Wufeng-Lower Silurian Gaojiabian Formations in Nanjing-Zhenjiang area. *Earth Sci. Front.* **2017**, *24*, 300–311. [[CrossRef](#)]
114. Semtner, A.-K.; Klitzsch, E. Early Paleozoic paleogeography of the northern Gondwana margin: New evidence for Ordovician-Silurian glaciation. *Geol. Rundsch.* **1994**, *83*, 743–751. [[CrossRef](#)]
115. Calvert, S.E.; Pedersen, T.F. Chapter Fourteen Elemental proxies for palaeoclimatic and palaeoceanographic variability in marine sediments: Interpretation and application. In *Proxies in Late Cenozoic Paleoceanography*; Hillaire-Marcel, C., De Vernal, A., Eds.; Elsevier: Amsterdam, The Netherlands, 2007; Volume 1, pp. 567–644. [[CrossRef](#)]
116. Caputo, M.V.; Landing, E.; Johnson, M.E. Ordovician-Silurian glaciations and global sea-level changes. In *Silurian Cycles: Linkages of Dynamic Stratigraphy with Atmospheric, Oceanic, and Tectonic Changes*; The New Press York State Education Department: Albany, NY, USA, 1998.
117. Johnson, M.E. Relationship of Silurian sea-level fluctuations to oceanic episodes and events. *GFF* **2006**, *128*, 115–121. [[CrossRef](#)]
118. Li, Y.; Zhang, T.; Ellis, G.S.; Shao, D. Depositional environment and organic matter accumulation of Upper Ordovician-Lower Silurian marine shale in the Upper Yangtze Platform, South China. *Palaeogeogr. Palaeoclimatol. Palaeoecol.* **2017**, *466*, 252–264. [[CrossRef](#)]
119. Liu, Z.; Algeo, T.J.; Guo, X.; Fan, J.; Du, X.; Lu, Y. Paleo-environmental cyclicity in the Early Silurian Yangtze Sea (South China): Tectonic or glacio-eustatic control? *Palaeogeogr. Palaeoclimatol. Palaeoecol.* **2017**, *466*, 59–76. [[CrossRef](#)]

Disclaimer/Publisher’s Note: The statements, opinions and data contained in all publications are solely those of the individual author(s) and contributor(s) and not of MDPI and/or the editor(s). MDPI and/or the editor(s) disclaim responsibility for any injury to people or property resulting from any ideas, methods, instructions or products referred to in the content.